CrossMark

Solar Wind Electron Pressure Gradients, Suprathermal Spectral Hardness, and Strahl Localization Organized by Single-point Measurements of $0.1\,\mathrm{nV\,m^{-1}}$ Ambipolar $E_\parallel$

Jack D. Scudder[1,2]
[1] Space Science Institute, Boulder, CO 80301, USA; JScudder@SpaceScience.org
[2] University of Iowa, Iowa City, IA 52242, USA

Abstract

A new, fast technique to measure the solar wind's ambipolar $E_\parallel$ routinely with 10% precision and accuracy is demonstrated using 4 yr of 1 au electron data from the Wind 3DP experiment. The 3DP electron instrument duty cycle determines $E_\parallel \simeq 0.1\,\mathrm{nV\,m^{-1}}$ from a single spectrum over much shorter time intervals than those requiring radial transits for pressure profiles. The measured weak electric field is invariably strong (in the dimensionless sense of Dreicer), with a modal value of $\mathbb{E}_\parallel = 0.8$, and positively correlated with solar wind speed, while $E_\parallel$ decreases with increasing wind speed. These observations establish across all solar wind conditions the nearly equal accelerations provided by $E_\parallel$ and coulomb drags on thermal electrons, a central hypothesis of the Steady Electron Runaway Model (SERM) for the solar wind. Filtered $E_\parallel$ observations successfully recover previously reported 1 au bulk speed dependence of electron temperature gradients. The filter screens for unstructured spherically symmetric solar wind (USSSW) conditions of solar wind theory. Outside USSSW conditions much shorter scaled pressure gradients (of both signs) and stronger $|E_\parallel|$ are observed predominantly in corotating regimes. Consistent with modeling by Dreicer and SERM, the observed spectral hardness of electrons at suprathermal energies is positively correlated with increasing local values of $\mathbb{E}_\parallel$ across the 4 yr data set. Virtually all *strahl* electrons, crucial to the electron heat flux, are shown to be confined *within* the local closed coulomb separatrix of each spectrum as determined using the locally measured value of $\mathbb{E}_\parallel$.

Unified Astronomy Thesaurus concepts: Plasma astrophysics (1261); Solar wind (1534); Space plasmas (1544); Interplanetary particle acceleration (826); Collision processes (2065)

1. Introduction

The in situ diagnosis of space plasmas increasingly attempts to characterize a wide set of physical parameters to help us understand their behavior. This set usually includes the DC and wave vectorial magnetic field $\boldsymbol{B}$; the velocity $\boldsymbol{V}$ of the center of mass; the two components of the unipolar electric field $E_\perp$ and vector electric waves; the three-dimensional velocity distributions of the electrons, protons, minor ions, energetic particles, and cosmic rays; and often imaging. The ancillary information allows moments through the pressure tensor and heat flux to be obtained for each species by numerical integration over $\boldsymbol{v}$. These in situ studies are then used to frame interpretations for the behavior of remote plasmas where diagnosis in this detail is not possible.

The DC magnetic-field-aligned parallel electric field $E_\parallel$ is routinely unavailable, not because it is theoretically unimportant but because of the extreme difficulties in measuring it. At 1 au this field can be theoretically estimated to be $\mathcal{O}(0.1)$ $\mathrm{nV\,m^{-1}}$, roughly *one million times weaker* that the smallest $E_\parallel = \mathcal{O}(0.1)\,\mathrm{mV\,m^{-1}}$ ever measured on spacecraft with long wire double probes. Sun phase variations of spacecraft sheaths already pose systematic problems for projecting out $E_\parallel$ below $0.1\,\mathrm{mV\,m^{-1}}$ levels. In extreme contrast, the solar wind's $E_\parallel$ component is one ten-millionth the size of the DC unipolar and more routinely measured solar wind electric field, $E_\perp = \mathcal{O}(2)\,\mathrm{mV\,m^{-1}}$. From mechanical alignments alone $E_\parallel$

cannot be determined by geometry after first measuring the total solar wind $\boldsymbol{E}$ field. Limited rough empirical estimates of $E_\parallel$ in the solar wind have been reported after fitting the witnessed electron pressure variation after moving $\simeq 0.5\,\mathrm{au}$ with a slow time resolution set by Kepler mechanics of the spacecraft trajectory.

Physically $E_\parallel$ plays a critical role in any inhomogeneous and thus astrophysical plasma. It is responsible for ensuring that charge density is nearly zero (i.e., quasi-neutrality) almost everywhere in the interconnected plasma system. In a very real sense $E_\parallel$ is the glue that gives a plasma the cohesiveness to be approximately described as a high-temperature quasi-neutral gas sharing many properties with those of uncharged gases. With their high temperatures, plasmas invariably conduct heat; however, undissuaded electrical currents generally accompany the heat flow. Such currents can disrupt quasi-neutrality and must be quenched by further adjustments of the local size and variation of $E_\parallel(\boldsymbol{x})$.

Ironically, $E_\parallel$ can also produce unexpected consequences for the nominal hydrodynamics of the center of mass of a hydrogenic plasma. When $E_\parallel$ strives to suppress current while permitting heat flow, it often does so by accelerating the positive ions and decelerating the negative electrons in such a way that the plasma's quasi-neutral gas center of mass moves in a favorable direction to elude the gravitational grasp of the proximate star.

Thus, the physics of $E_\parallel$ is intimately intertwined with a challenging unsolved problem about astrophysical plasmas: a quantitatively viable plasma description for the flow of heat in the strong gradients that are required in astrophysical plasmas and the ultimate cause for the formation of stellar winds that lift gravitationally bound ions to be free of the star's grasp. Such

behavior and $E_\parallel$ would not occur if the plasma were a sea of bound neutral hydrogen atoms; such a neutral atmosphere would remain bound to the star where it formed.

Recent attempts for this astrophysical problem involving plasmas have drawn attention to the role of the strength of $E_\parallel$ in creating the ubiquitously observed leptokurtotic nonthermal electron distributions in the solar wind; they are suggested to be more efficient at supporting heat transport with less strain on the maintenance of quasi-neutrality and zero current (Scudder 2019b). Further, since $E_\parallel$ must occur in astrophysics because of its inhomogeneity, and because $E_\parallel$ makes distributions nonthermal in lowest order, the Maxwell−Boltzmann distribution is unlikely to be the lowest-order velocity distribution in space plasmas. This sequence of arguments constitutes a redirection for the much-needed transport recipes in space plasmas (Scudder 2019c).

Kinetically the *strength*/importance of a given $E_\parallel$ can be gauged by comparing its electric force on any electron to the proton coulomb collisional drag force on a typical electron. This concept is due to Dreicer (1959, 1960), who introduced the size of a *critical* field, E_c, that has since been used by other authors to mean something different. In this paper Dreicer's E_c electric field is denoted by E_D. It is conceptually defined in terms of the ion drag felt by an electron moving with the electron thermal speed, w_e, defined by $m w_e^2 = 2\,kT_e$ and the coulomb rate in a plasma for ion-induced momentum loss of that speed electron, symbolically noted as $\nu(w_e)$. Because the collisional rates in a plasma are strongly speed dependent, the preceding definition involves specific rates for which there is no ambiguity that are completely delineated in Equation (A1). For a proton plasma E_D is defined by

$$eE_D \equiv m_e w_e \nu(w_e), \tag{1}$$

which can be rewritten in terms of fundamental plasma constants in Equation (A1) and other ways that are easier to remember, such as

$$eE_D = \frac{2kT_e}{\lambda_{\mathrm{mfp}}}; \quad \lambda_{\mathrm{mfp}} \equiv \frac{w_e}{\nu(w_e)}, \tag{2}$$

also derived there.

With this definition Dreicer suggested the numerical ratio of the magnitude of the parallel electric field to E_D as a *measure of the strength* of $E_\parallel$. In this paper the symbol $\mathbb{E}_\parallel$ is used for this nonnegative *dimensionless strength*:

$$\mathbb{E}_\parallel \equiv \frac{|E_\parallel|}{E_D} \gtrsim 0. \tag{3}$$

In this form the strength of $E_\parallel$, the numerical size of $\mathbb{E}_\parallel$, indexes the relative importance between the unimpeded accelerations of $E_\parallel$ and the collisional deceleration represented by proton coulomb drag on a thermal speed electron, w_e. Thus, very small $\mathbb{E}_\parallel \ll 1$ implies that coulomb collisional drag has overwhelmed the force produced by $E_\parallel$. $\mathbb{E}_\parallel \simeq 1$ suggests a more equal competition, while $\mathbb{E}_\parallel \ggg 1$ delineates the domain where the plasma is nearly collisionless. True thermodynamic equilibrium has a vanishing strength electric field: $\mathbb{E}_\parallel = 0 = E_\parallel$. A *strong* parallel electric field is one where the dimensionless parallel field is around 1, namely, $\mathbb{E}_\parallel = \mathcal{O}(1)$, and collisions are significantly involved in the balances necessary for zero current and quasi-neutrality.

Dreicer developed other properties of plasmas in the presence of parallel electric fields, some specialized for the spatially uniform laboratory regime. One specialized conclusion concerns what happens in uniform plasma when $\mathbb{E}_\parallel$ exceeds specific values ($\mathbb{E}_\parallel > 0.43$) that do not apply in the astrophysical context because of the prominent role of inhomogeneity and heat flow not considered in Dreicer's simpler models. This threshold for uniform lab plasmas explains the observations seen *there* of the onset of *bulk runaway*, with nearly all electrons slipping at or above the electron thermal speed through the ions, with friction decreasing as that slippage continues to grow secularly. At present it is not known how to define the bulk runaway regime for inhomogeneous astrophysical plasmas. In this paper no boundary is identified that corresponds to Dreicer's $\mathbb{E}_\parallel = 0.43$ transition into bulk runaway.

For $\mathbb{E}_\parallel < 0.43$ Dreicer demonstrated that *kinetic runaway* still occurs in uniform plasmas for some speed electrons but that the total ion drag on *all* speed electrons could balance the electric force, allowing a stationary *ohmic* balance to characterize the asymptotic state. The Steady Electron Runaway Model (SERM) suggests the slippage of the thermal core to be this type of response in the solar wind and that the kinetic runaway enabled by the size $\mathbb{E}_\parallel$ is the explanation of the number fraction of the ubiquitously nonthermal electron velocity distribution function (eVDF) reported in the solar wind for the past 50 yr. Net current flow is forestalled by return currents involving the non-core part of the eVDF in much the same way as determined by Scudder & Olbert (1979).

The electron momentum equation's leading-order form suggests (Rossi & Olbert 1970) that $\mathbb{E}_\parallel$ is half the electron pressure Knudsen number, $\mathbb{K}_{P_{e\parallel}}$, viewed as the ratio of mean free path for the thermal speed electron, λ_{mfp} (see Equation (A1)), divided by the characteristic scale length $\mathcal{L}_\parallel$ of gradients along the magnetic field given explicitly in Equation (22). Estimates in astrophysical plasmas of λ_{mfp} and typical spatial gradient scales suggest that the Knudsen number is commonly $\mathcal{O}(1)$. Accordingly, the electron momentum equation implies that the attendant $E_\parallel$ will be strong, $\mathbb{E}_\parallel \simeq \mathcal{O}(1)$, and be common in astrophysics (Scudder 1996; Meyer-Vernet & Issautier 1998; Meyer-Vernet 2007; Scudder & Karimabdi 2013).

The general idea that finite $\mathbb{E}_\parallel$ promotes a subset of the electrons into *local runaway* is still a meaningful insight even in the astrophysical context. Local runaway is a uniquely plasma phenomenon for any finite $\mathbb{E}_\parallel$; it is made possible by the coulomb scattering rate being inversely and strongly dependent on the relative speed of the projectile and target. In the presence of a parallel electric field a minimum-speed electron always exists above which the push of $E_\parallel$ transfers more energy than the electron loses from coulomb scattering. At and above this speed increases by $E_\parallel$ of the kinetic energy continue growing, locally always exceeding the increasingly smaller collisional losses; at first it would appear that the electron energy grows secularly by the energy supplied by $E_\parallel$. In reality, this secular behavior (i) generally only occurs for a few electrons and (ii) persists only until previously neglected processes interdict the simple picture of a nonradiating particle in a uniform infinite plasma with a fixed parallel electric field scattering off of structureless ions of negligible speed.

The need for quasi-neutrality ensures that $\mathbb{E}_\parallel = \mathcal{O}(1)$ is expected to be omnipresent in astrophysics; thus, the local

runaway process is always at work (Dreicer 1959, 1960; Scudder 1996, 2019c), not only for the solar wind but more generally in astrophysics. By this argument the observed, ubiquitous, nonthermal electrons of the solar wind should also be the expected normal behavior for remote astrophysical plasmas rather than the exception.

2. This Paper

This paper describes a new technique to routinely measure $\mathbb{E}_\parallel$ at one point in space in the solar wind by asking the electrons what parallel electric field they sense; the technique's high time resolution, compared to that of the pressure gradient $\mathbb{E}_\parallel$ determinations, arises because the proposed measurement does not require waiting for the traversals of adequate distances to infer weak spatial gradients. Here $E_\parallel$ and $\mathbb{E}_\parallel$ are determined after performing operations on a specific magnetic-field-aligned one-dimensional cut of the empirically measured eVDF recovered using the intermediate Wind 3DP data products for 1995–1998 recently published and tabulated (Salem et al. 2021).

The new technique derives its sensitivity to $\mathbb{E}_\parallel$ by respecting Dreicer's conclusions about the strong speed dependence of coulomb collisions: for any finite $\mathbb{E}_\parallel$ there is a lowest energy range of the eVDF ($E^* < 3kT_e/\mathbb{E}_\parallel$) where collisions are so vigorous that the eVDF should be no more complicated than a drifting, nearly isotropic Maxwellian. The measurement interrogates the *observed* eVDF along the magnetic field in the direction opposite to the heat flux and quantifies where the leptokurtic eVDF has departed from its drifting mildly anisotropic Maxwellian form at lower energies. This determination is discussed in detail in Section 4.

Using this technique, the size of $\mathbb{E}_\parallel$ is surveyed across 4 yr (1995–1998) using 96 s resolution solar wind data collected at the forward Lagrangian point by the Wind 3DP experiment (Lin et al. 1995). Each *measurement* of $\overline{|\mathbb{E}_\parallel|}$ is the average of two systematically different *determinations* of $\mathbb{E}_\parallel$. The differences of these determinations from the reported average are used to document the average achieved *reproducibility/precision* of the reported *measurement* for the single 3D eVDF used. Four years of data suggest that $\overline{|\mathbb{E}_\parallel|}$ has a *reproducibility/precision* of better than 10%.

Aware that high reproducibility *can* result from systematic error, a second stage of validation is undertaken (Section 9) to document whether six theoretically motivated correlations between $\overline{|\mathbb{E}_\parallel|}$ and other plasma observables could be corroborated using other measurements. These correlations involve testing quantitative agreements between the expected size of pressure profile power-law exponents based on $E_\parallel$ and those (i) forbidden, (ii) allowed, and (iii) likely for an expanding fluid like the solar wind; (iv) determining the most likely found radial power-law exponents for the electron pressure or temperature for the unstructured spherically symmetric solar wind (USSSW) of solar wind theory; and (v) the recovery of the bulk speed dependence of these radial power laws using $E_\parallel$ that match quantities recently published using pressure profiles traversed in the wind (Maksimović et al. 2020). The role of systematic error (vi) in the final test of accuracy is also shown to be small by contrasting the decay of the experimental corroboration under an alternate suggestion for the interpretation of the break point energy scaling (see Figure 21).

These last three tests are especially sensitive to the certification of the *calibration/accuracy* of the reported values
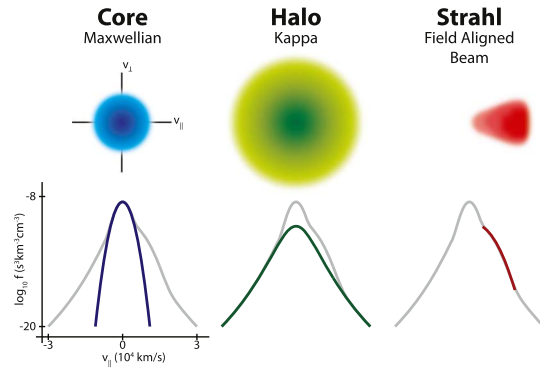
Figure 1. Cartoon representation of solar wind eVDF showing traces of field-aligned cuts (bottom) and pitch-angle distributions (top) of the *thermal core*, the *suprathermal halo*, and *strahl* subcomponents. Lower colored traces indicate the subcomponent's location in the overall (gray) composite eVDF's magnetic-field-aligned profiles. Once the core and halo fits are performed excluding the heat flux supporting bulge along the magnetic field, the total eVDF (gray profiles and their extensions in pitch angles) is reduced by the predictions of the core and halo fits, yielding the residual size and location of the suggested *strahl* component. The strahl's bulge is found along the empirical heat flux direction determined from the entire model-independent assay of the eVDF. Courtesy M. Pulupa, http://sprg.ssl.berkeley.edu/~pulupa/.

of $\overline{|\mathbb{E}_\parallel|}$, establishing that the Wind-SERM analysis presented here determines $\overline{|\mathbb{E}_\parallel|}$ and hence $\overline{|E_\parallel|}$ at the 0.1 nV m^{-1} level with a better than 10% accuracy.

Four multiyear correlations provide arguments that the measured values of $E_\parallel$ are geophysical and consistent with their theoretical expectations: (i) size and bulk speed dependence of electron temperature gradients compared to these same quantities from pressure gradient time series, (ii) $\mathbb{E}_\parallel$ positively correlated with solar wind speed, (iii) suprathermal spectral hardness positively correlated with $\mathbb{E}_\parallel$, and (iv) strahl's almost exclusive localization within the most stringent closed coulomb runaway separatrix determined by locally measured $\mathbb{E}_\parallel$.

3. The Nonthermal Solar Wind eVDF

Many different experimental groups have modeled the velocity space electron probability distribution $f_e(\mathbf{v})$ in the solar wind as a superposition of peaked phase-space subcomponents with their own different densities, characteristic energies, and peculiar magnetic-field-aligned drift speeds (Montgomery et al. 1968; Feldman et al. 1975; Rosenbauer et al. 1977; Ogilvie & Scudder 1978; Pilipp et al. 1987; Larson et al. 2000; Salem et al. 2003, 2021; Maksimović et al. 2005; Štverák et al. 2009, 2015; Halekas et al. 2020). A cartoon in Figure 1 relates the names, phase-space shapes, and relative locations of these subcomponents with commonly adopted names *core*, *halo*, and *strahl*.

All subcomponents are observed to possess equal cross-field drifts, consistent with a magnetized plasma; sketches of the magnetic-field-aligned cuts of these subcomponents are shown in the bottom row of the cartoon, with colored traces superposed on the full parallel trace of the entire eVDF.

The model-independent $f_e(\mathbf{v})$ is *skewed*, *nonthermal*, and *leptokurtic*; its prominent heat flow reflects its skewness, the departures from a parabolic profile for $\ln f_e(v_\parallel)$ indicate that it is nonthermal, and its overpopulated suprathermal population justifies its being leptokurtic. The heat is observed to flow along the magnetic field direction, usually away from the Sun and with the same field-aligned bias as the displacement of the

strahl subpopulation in the ion's rest frame as shown in Figure 1.

The fit parameters of the subcomponent modeling and nearly model-independent direct numerical integration of the eVDF separately support the idea that the *net* charge number flux of the superposition of these electron subcomponents matches that observed for the ions. This evidence for the Wind 3DP analysis has recently been published (Salem et al. 2021) and verified for this data set by the author. Multiple experimental groups have suggested that the wind as a whole does not represent a field-aligned current, despite being permeated by a theoretically required nonzero parallel electric field (Lemaire & Scherer 1971).

The measured 3D eVDF surface is often modeled by an optimized superposition of overlapping subcomponents shown in Figure 1; shape coefficients c_k are adjusted to maximize the agreement of the model with the observed eVDF that is well sampled in energy and solid angle by Wind 3DP (Lin et al. 1995). After optimizing these coefficients, the value of the eVDF at any given velocity space location can be obtained as

$$f_{e,\text{obs}}(\boldsymbol{v}) \simeq \Sigma_k F_k(\boldsymbol{v}, \boldsymbol{c}_k). \tag{4}$$

Typically the observed subcomponents for the thermal core and suprathermal halo are modeled as having even parity in parallel velocities about their own rest frame and gyrotropic about $\hat{\boldsymbol{b}}$. As described below, the strahl assay on Wind is formed by subtraction of gytropic models and is thus modeled as gyrotropic; generally the strahl determined in this manner contains a skewness in its own rest frame (Salem et al. 2021). The lowest χ_ν^2 for the best choices of the F_k values produces a skewed, heat-conducting eVDF as the result of best-fit subcomponent rest frames sliding independently along $\hat{\boldsymbol{b}}$.

Since the early Vela and Interplanetary Medium Platform measurements, it has been noted that subcomponent fits of this type yielded a composite $f_e(\boldsymbol{v})$ that could replicate within errors the model-independent lower moments (through the heat flux) of the eVDF determined *without* subcomponent fitting. After including the strahl modeling, the more recent and refined resolution Wind 3DP data set has this property as well (Salem et al. 2021).

A typical modeling approach forms the sum in Equation (4) using an anisotropic bi-Maxwellian *core* for low proper frame energies, together with an anisotropic κ *halo* distribution (Olbert 1968) for suprathermal energies; a phase-space-localized *strahl* component is usually identified astride the heat flux pitch angles of the eVDF (Rosenbauer et al. 1977; Feldman et al. 1978; Ogilvie & Scudder 1981; Pilipp et al. 1987; Maksimović et al. 2005; Štverák et al. 2009; Halekas et al. 2020; Salem et al. 2021).

The strahl contribution was identified in Wind 3DF by finding phase-space locales where the predictions of the superposed core and halo fits (determined by fits outside the heat flux pitch angles) were unable to predict the observed fluxes. Generally these strahl contributions were sought within the white rectangle in Figure 2.

In the best-fit representations all three components drift along $\hat{\boldsymbol{b}}$, but with different speeds in the ion rest frame. The core drift in the ion frame is ultra-subsonic, the halo subsonic, and the strahl mildly transonic (see below, however); in all cases the reference thermal speed is that of the subcomponent. Except for the strahl, these drifts are difficult to perceive in the bottom row of cartoon profiles in Figure 1; however, the drifts
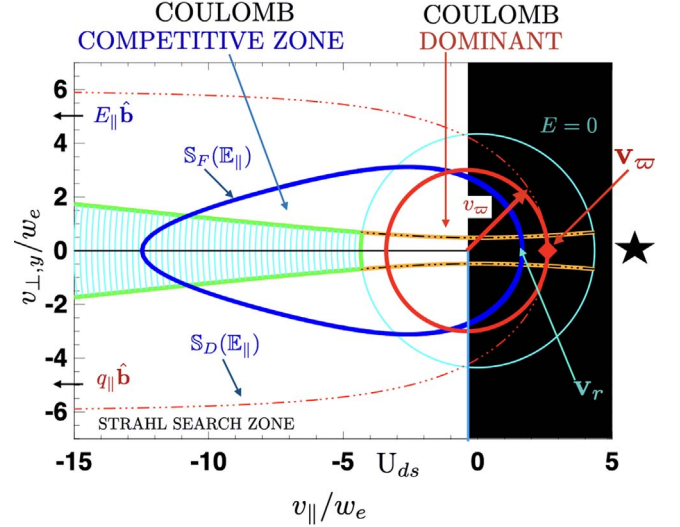
Figure 2. Theoretical boundaries anticipated for the solar wind eVDF in the rest frame of the Sun. Exospheric boundaries: cyan circle; total energy $E = 0$: orange hyperbolae; exospheric strahl: green subset of hyperbola. Coulomb collisional structures: (i) red circle (centered at the ion rest frame) of speed radius, v_ϖ: this is the outer speed limit of Dreicer's domain of coulomb *collisional dominance*; (ii) blue separatrix, $\mathbb{S}(\mathbb{E}_\parallel)$, the boundary between collisionally inward recycled electrons and promoted runaways that have passed outward across $\mathbb{S}$. $E_\parallel\hat{\boldsymbol{b}}$ and $q_\parallel\hat{\boldsymbol{b}}$ are generally aligned as shown, while the electric force on the electron opposes this common direction and is generally sunward. A complementary section of the *observed* eVDF along the magnetic field is shown vs. speed in Figure 3 and magnified in Figure 4, and vs. kinetic energy in Figure 5.

are clearly measurable, are coordinated, and suggest that the entire electron part of the plasma does not drift in the ion rest frame.

In the solar wind the canonical heat flow direction is along the magnetic field; based on statistical mechanics, the direction of $E_\parallel\hat{\boldsymbol{b}}$ is expected to be aligned with $q_\parallel\hat{\boldsymbol{b}}$. The Drude arguments (1900a, 1900b) based on collisions and Dreicer's (1960) update for a plasma and the SERM model (Scudder 2019b) suggest that the magnetic-field-aligned drift of the thermal electrons (in the ion rest frame) should be opposite to $E_\parallel\hat{\boldsymbol{b}}$, yielding the interlinked directional expectations:

$$\frac{q_\parallel}{|q_\parallel|} = \frac{E_\parallel}{|E_\parallel|} = -\frac{U_{c,\parallel}}{|U_{c,\parallel}|} = \frac{U_{h,\parallel}}{|U_{h,\parallel}|} \simeq \frac{U_{s,\parallel}}{|U_{s,\parallel}|}. \tag{5}$$

These relations (except those involving $E_\parallel$) are well documented by extensive solar wind observations as shown in Salem et al. (2021) and multiple references cited therein.

3.1. Speed and Pitch-angle Space of the eVDF

The speed–pitch-angle distributions routinely inferred in the solar wind are suggested by the top row of insets in Figure 1. The observed extent of these eVDF subcomponents in this plane is often used in theoretical discussions of their origin. In the *collisionless exospheric* limit, boundaries can be determined in this plane for kinematic access of electrons, as they can find their way through the electrostatic and magnetic field variations while remaining quasi-neutral. Because coulomb collisions are always present, there are also unanticipated boundaries in this speed–pitch-angle plane with ultimate rationales more general than the boundaries formulated by collisionless exospheric arguments.

Throughout this discussion it should remain clear that the subcomponent boundaries and extents of the pitch-angle distributions in the top row of the cartoon in Figure 1 are not model independent but are inferences where these subcomponent functions *dominate* the composite, observed eVDF. What is established by this composite fit is an optimized superposition of functions that replicated the measured eVDF well. Such considerations imply that phase-space boundaries or other signatures have to be experimentally determined from the entire eVDF as delineated by the observations. Even the best vernier instrumentation need not have flux variations along any given needed direction in the three-dimensional velocity space. The use of a composite fit allows subsequent analysis to obtain the best synthesis of the eVDF along desired phase-space paths, making the best use of the overdetermination present in the composite fit to the entire eVDF while refraining from plate-like interpolations of the raw inferred eVDF from the corrected pixel fluxes returned in telemetry.

Before discussing how to measure $E_\parallel$, we describe in Figure 2 the locations of various electron phase-space boundaries alluded to in the exospheric literature and some caused by collisions. Although this figure is a quantitatively constructed version of the phase space shown in the top row of Figure 1, it is still a simplified polar diagram of the speed–pitch-angle space dependencies of the observed solar wind electron eVDF.

The figure's velocity space origin is the Sun's rest frame; particles going toward the Sun are moving to the right, toward the black star in the diagram. In typical situations the *observed* solar wind heat and number fluxes flow away from the Sun, to the left in this figure. In this example the wind is flowing at $400\,\mathrm{km\,s^{-1}}$.

The exospheric boundaries key on the Sun's rest frame for their parallel origins, while the collisional boundaries usually are centered at the local solar wind's rest frame (as, e.g., the center of the red circle at the solar wind velocity).

The cyan circle, centered on the Sun's rest frame, encloses the negative total energy trapped particles of exospheric theory, and *some of* its occupants have come to be associated with the *thermal core* of the routinely observed solar wind eVDF. Electrons found on the bounding $E = 0$ cyan boundary in exospheric theory have a speed v_ϕ related to the size of the *exosphericist's* electrical potential at that spatial position given by $-e\Phi_{\mathrm{exo}}(r) = \frac{1}{2}mv_\phi^2$, where the zero of the potential is assumed to be at infinity. A source of confusion is the relation of any exospheric electrical potentials foreseen and those electric potentials that occur in a plasma where collisions occur. Given the approximate character of the exospheric model, these potentials are probably not identical.

The *strahl* of collisionless exospheric theory occupies an unbounded positive total energy ($E > 0$) regime between the green extensions of the two orange hyperbolas with superposed black dashed–dotted lines. Mathematically the strahl of exospheric theory occupies the phase space contoured with cyan level curves between the extended asymptotes at speeds above v_ϕ associated with $E > 0$. The reported strahl signatures generally occur moving away from the Sun on open field lines and almost always in the direction of the moment heat flux.

In exospheric theory the total $E = 0$ boundary (cyan circle) delimits the smallest speed isocontour of the *theoretical exospheric strahl* subcomponent. Commonly the strahl is identified by its rather sharp pitch-angle distribution centered about the moment heat flux direction of the eVDF. Because of the difficulty of measuring the electrical potential, the reported strahl eVDF signatures are seldom, if ever, certified as residing above the $E = 0$ boundary.

Theoretically the strahl in exospheric theory carries all the number flux and heat flow carried by the electrons. The *remainder* of the phase space is modeled as occupied by electrons whose distributions are even functions of their parallel speed described in the Sun's rest frame. In exospheric theory these *remainders* do not contribute to the odd moments of the electrons. Since the observed thermal core electrons are generally viewed as having $E < 0$ but still observed to have a flow speed nearly that of the ions, the exospheric neglect of collisions is surely incomplete. Additionally, there is the possibility that collisionally moderated heat flow signatures will also involve field-aligned skewness that could be misconstrued as exospheric strahl phenomenology (see Figure 4 in Scudder 2019b).

The white shaded rectangle in this figure indicates the general vicinity of the eVDF where Wind 3DP strahl searches may have found signatures (but not its precise boundary). The outline of this inferred *strahl search zone* will vary based on the energy dependence of the inferred pitch-angle features identified (see Figure 1). The generic rectangular region is called out here as the *strahl search zone* to emphasize that signatures identified as strahl may not be an unequivocal measurement of a surviving *exospheric strahl* component. This ambiguity is discussed in more detail below in conjunction with the strahl parameters determined from the 3DP Wind observations and must be kept in mind for eVDF features identified as *the* strahl in other surveys.

Many authors have suggested that the nonstrahl $E > 0$ population is populated by various wave–particle effects spawned by the erosion of the collisionless strahl. In the context of Figure 2 and the SERM model, promotion by $\mathbb{E}_\parallel$ outward across the separatrix $\mathbb{S}(\mathbb{E}_\parallel)$ is an alternate but *omnipresent* collisional source for halo electrons at pitch angles outside of *the* strahl zone of exospheric theory that needs further consideration. In addition, considerations of coulomb collisions suggest that all electrons inside of $\mathbb{S}$ and outside of the red circle are in a constant state of interpenetrating circulation (see Fuchs et al. 1986); this circulation represents a significant *collisional* source for the halo not produced by the above-mentioned wave–particle process.

The finite coulomb collision frequency (ignored by exospheric theory) introduces three other boundaries in Figure 2: (i) Within the red circle of kinetic energy $\mathcal{E}_\varpi = m_e v_\varpi^2/2$ *centered on the ion rest frame* is the domain where electron–proton collisions are so strong that Dreicer argued that the eVDF should at worst be *a convecting, nearly isotropic Maxwellian*; Dreicer's separatrix $\mathbb{S}_D$ is indicated by the open red dashed wind-sock boundary that encloses a larger volume in velocity space than the blue separatrix labeled $\mathbb{S}_F$ due to Fuchs et al. (1986). Dreicer's minimum speed, v_ϖ, for promotion into kinetic runaway is at the red diamond at the base of the wind sock derived considering only ion drag in competition with $E_\parallel$ acceleration. The blue $\mathbb{S}_F$ curve was derived (Fuchs et al. 1986) considering energy-loss effects in addition to those considered by Dreicer; in a proton plasma its minimum runaway speed occurs at the green speed labeled v_r

and is given by Fuchs et al. (1986):

$$v_r \simeq 0.9 \frac{3^{1/4}}{\mathbb{E}_{\parallel}^{1/2}} \quad \text{Fuchs et al. (1986)}$$

$$v_{\varpi} = \frac{3^{1/2}}{\mathbb{E}_{\parallel}^{1/2}} \quad \text{Dreicer (1960)}$$

$$v_r = 0.683 v_{\varpi}$$

$$v_* = \sqrt{\zeta} v_{\varpi}. \tag{6}$$

In this paper we will explore both the Dreicer and Fuchs et al. $\mathbb{S}$ boundaries in our desire to estimate $\mathbb{E}_{\parallel}$. Since they both have the same functional scaling on $\mathbb{E}_{\parallel}$, a consistent choice devolves on the accuracy of the ultimate $E_{\parallel}$ that is implied, since with Fuchs the inferred $E_{\parallel}$ predicts a weaker ambient electric field than Dreicer's formulation:

$$E_{\parallel}^{\text{Fuchs}} = 0.467 E_{\parallel}^{\text{Dreicer}}$$

$$E_{\parallel}(\zeta) = \zeta E_{\parallel}^{\text{Dreicer}}, \tag{7}$$

where an arbitrary factor ζ off of Dreicer's prediction is introduced to accommodate both choices in Equation (6). (ii) Both $\mathbb{S}$ boundaries are asymmetric in $v_{\parallel}$ but cylindrically symmetric about $\boldsymbol{B}$; the runaway immune region is open in Dreicer's separatrix but closed in the blue curve of the Fuchs separatrix, $\mathbb{S}_F$. Both separatrices enclose the ion flow rest frame, being elongated on the heat flux and strahl's side of the origin.

In the presence of *any* $E_{\parallel}$ some electrons will be promoted from inside to outside these separatrices, energizing them to local *runaway* status. When launched in this manner, electrons locally gain energy secularly from the parallel electric field that exceeds their losses to collisions. Promotion to runaway status is most favorable in the direction of the electric force on electrons, but a finite rate for promotion exists at all pitch angles, including the strahl's direction of exospheric theory's wedge of pitch angles (Fuchs et al. 1986). Electrons within both $\mathbb{S}$ boundaries are strongly recirculated among themselves by coulomb collisions, including interacting between electrons inside the strongly collisional region (Dreicer 1960; Fuchs et al. 1986).

Runaway promotion cannot explicitly occur in the steady collisionless exospheric theory. Recent clarifications of the details for achieving formally exospheric winds with high velocities have shown the importance and necessary role of collisional access into otherwise inaccessible collisionless orbits (Zouganelis et al. 2005). In the exospheric modeling these effects are suggested to be necessary, together with nonthermal boundary conditions, to achieve quasi-neutral current-free high-speed winds exceeding $800 \, \text{km s}^{-1}$. Thus, even the collisionless picture has tacit inclusion of collisions when needed.

4. Measuring $v_{\varpi}(\mathbb{E}_{\parallel})$

By consensus, the eVDF subcomponent with the highest ambient plasma phase-space density occurs at the lowest energies in the solar wind frame (see Figure 1), being hotter than and distinguishable from secondaries and photoelectrons. With the strong inverse speed dependence of the coulomb scattering, the core electron subcomponent, as nearest the ion bulk velocity, was identified in the SERM model
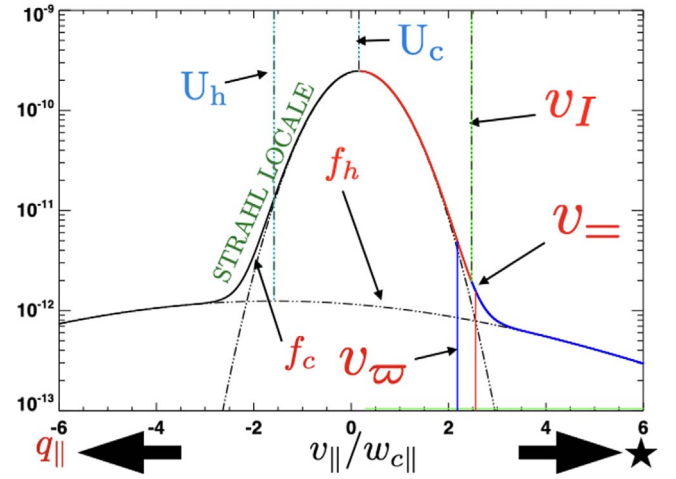
Figure 3. Figure shows the full magnetic-field-aligned semilogarithmic slice $f(v)$ of the ubiquitously observed, nonthermal, and skewed solar wind eVDF, $f_e(\boldsymbol{v})$, using Equation (9). Dashed–dotted curves reflect the core and halo terms in Equation (9). When present, the strahl would occur with $v < 0$ and within the green lettered area on the composite profile. Three closely located candidate boundaries v_{ϖ}, v_I, and $v_=$ are identified here and magnified in Figures 4 and 5.

(Scudder 2019b) as the overdamped population of Dreicer (1959, 1960), Scudder & Olbert (1979), and Fuchs et al.(1986).

Consistent with Dreicer's modeling, the solar wind electron core is only weakly anisotropic and is observed to drift in the direction of the parallel electric force (away from the heat flux) and come to a quasi-time stationary *antisunward* drift in the ion rest frame. Such a model is the general solution of the Fokker–Planck equation in the presence of finite $\mathbb{E}_{\parallel}$ that is not *too* large. It is precisely the model Dreicer suggested would occur in his collisionally overdamped regime. Also consistent is that the steady core drift in the ion rest frame is observed to be well below the core's thermal speed.

The identification of the core subpopulation of the observed eVDF with Dreicer's overdamped population is crucial leverage for the technique presented below for measuring $E_{\parallel}$ in the plasma; it involves finding the minimum field-aligned speed, $\sqrt{\zeta} v_{\varpi}$, *at or within the sunward extreme of the red circle in Figure 2*.

5. Ambipolar $E_{\parallel}$ from Measured eVDF

We find $v_{\varpi}(\mathbb{E}_{\parallel})$ by interrogating the magnetic-field-aligned cut of the modeled eVDF given by $f(v_{\parallel}) \equiv f_e(-\boldsymbol{v} \cdot q_{\parallel} \hat{\boldsymbol{b}} > 0)$, where the direction selected is a ray parallel to the local magnetic field direction but *opposite* to the heat flux. In this way $f(v_{\parallel})$ focuses on $v_{\parallel} \gtrsim 0$ particles that move along the direction of the *local parallel electric force* on the electrons, $-|e|E_{\parallel} \hat{\boldsymbol{b}}$.

For the remainder of this paper we use $f(v_{\parallel})$ without the subscript e and with a scalar argument to denote preferentially this cut; such a section should pass through $v_{\varpi} > 0$ and is shown in Figure 3, and it should be contrasted with the full pitch angle of velocity space shown in Figure 2.

The generally sunward cut of the eVDF along the magnetic field, $f(v_{\parallel})$, has only nonzero model contributions from the core's Maxwellian and halo's kappa subcomponents, since the strahl term, F_{strahl}, is not present (see Figure 1) on the side of the eVDF opposite the heat flow's skew. If the strahl component were present, it would be found in the vicinity of the green lettering in Figure 3.
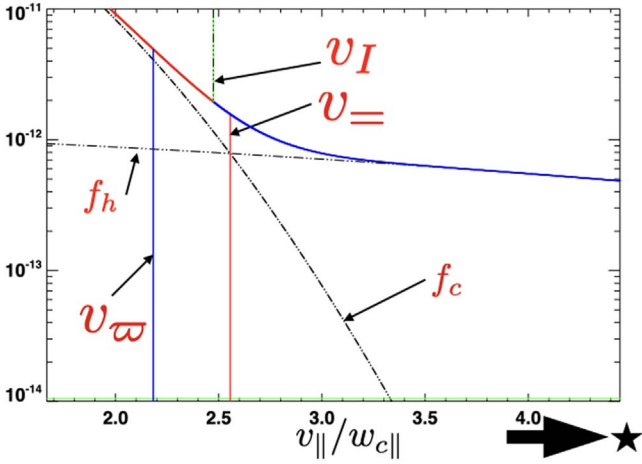
Figure 4. This figure is a magnification of the sunward-propagating portion of Figure 3 focusing on the candidate boundaries. The separation of the red, negative curvature part of $f(v_\varpi)$ from $f_c(v_\varpi)$ is clearly shown. The color-coding and boundary candidates are retained across Figures 3–5 discussed together in the text.

Figure 5. This figure is a variant of Figure 4, requested by the referee, that magnifies the leptokurtic transition in semilogarithmic format vs. *kinetic energy*, showing its *slightly* different *but still smooth* appearance. The corresponding vertically marked kinetic energies of this figure $\mathcal{E}_x = m v_x^2/2$ remain distinct in this format, as do their related speeds that label the corresponding locations in Figure 3. Color-coding has been preserved across Figures 3–5.

Accordingly, using the modeled parameters of the composite fit to the eVDF in Equation (4), the best analytical synthesis of the observed eVDF along the direction moving toward the Sun (actually along $-q_\parallel \hat{\boldsymbol{b}}$) will have the form

$$f(v > 0) \simeq f_c(v) + f_h(v) \text{ where}$$

$$v \equiv -\frac{\boldsymbol{v} \cdot \boldsymbol{q}_e}{|\boldsymbol{q}_e|} = -\boldsymbol{v} \cdot \frac{E_\parallel \hat{\boldsymbol{b}}}{|E_\parallel|} > 0. \tag{8}$$
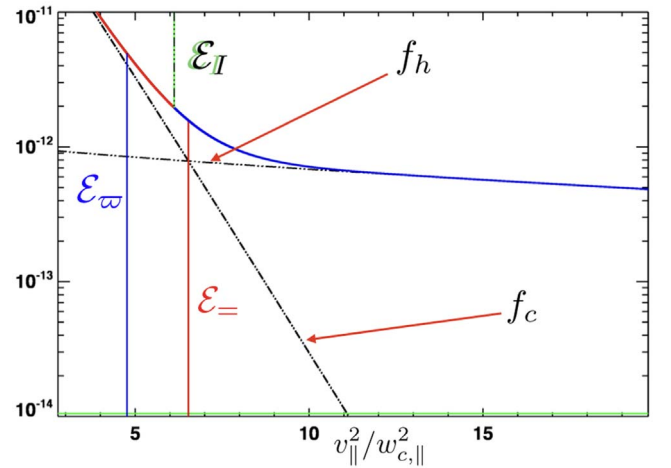
With these conventions, if the heat flows away from the Sun, it would be accompanied by the indicated sunward core drift with positive parallel speed $v = U_c > 0$ (in the ion frame) and the halo drift speed consistently negative $U_h < 0$.

The profile $f(v)$ for each spectrum (1995–1998) acquired by Wind 3DP is reconstructed here using the eVDF fit parameters for the subcomponents consistent with NASA's Open Data Policy as interpreted by Max Bernstein, NASA HQ. Statistical properties of the electrons characterized in this data set have already been discussed and summarized in tabular form in a recent publication (Salem et al. 2021).

Thus, the profile used for analysis $f(v)$ along $-q_\parallel \hat{\boldsymbol{b}}$ will include the minimum runaway speed v_ϖ having the form

$$f(v) = \frac{n_c}{\pi^{3/2} w_{c,\parallel} w_{c_\perp}^2} \exp\left[-\frac{(v - U_c^*)^2}{w_{c,\parallel}^2}\right]$$

$$\times \frac{n_h A(\kappa)}{\pi^{3/2} w_{h,\parallel} w_{h_\perp}^2} \left[1 + \frac{(v - U_h^*)^2}{\kappa w_{h,\parallel}^2}\right]^{-(\kappa+1)}, \tag{9}$$

where $v > 0$ and $A(\kappa) = \Gamma(\kappa+1)/(\Gamma(\kappa - 1/2)\kappa^{3/2})$ guarantees that n_h is the number density of the entire κ subcomponent, despite its non-Maxwellian shape. Since the observations characterize the drifts of eVDF components relative to the ion rest frame, the drifts in Equation (9) are actually taken to be $U_c^* = |U_{c,\text{fit}}|$ and $U_h^* = -|U_{h,\text{fit}}|$ provided that the spectrum fit values satisfy $U_{c,\text{fit}} U_{h,\text{fit}} < 0$ and are thus physical. Since $f(v)$ is a magnetic-field-aligned cut, the transverse part of the fitted eVDF has been evaluated at $v_\perp = 0$.

A composite semilogarithmic profile of shape $f(v)$, similar to that found in the solar wind, has already been shown in Figure 3. A magnified detail of this $f(v)$ is shown in Figure 4 using the same color codes, line coloring, and labeling conventions. It details the transitions in the leptokurtic profile precisely where the halo subcomponent fraction perceptibly competes with the core contributions for the observed composite $f(v)$.

The cut of the composite eVDF for the sunward-moving electrons is shown in red where its curvature is negative and in blue where it is positive. Three boundaries with decreasing speed, $\{v_=, v_I, v_\varpi\}$, are indicated in these figures.

The boundary speed, labeled v_I, between regions of opposite curvature is the *point of inflection*. The boundary at $v_=$, often called the *hinge point*, is where the core and halo subcomponents contribute equally to the total observed phase-space density. The boundary at v_ϖ has been computed for this spectrum and will be identified below with Dreicer's minimum speed for runaway, but at present it satisfies one of Dreicer's attributes: it is in a region of negative curvature, and thus $v_\varpi < v_I$, placing it below the inflection point, v_I. The inflection point for $\ln f(v)$ has the implicit geometrical definition from calculus:

$$\left.\frac{d^2 \ln f(v)}{dv^2}\right|_{v_I} = 0. \tag{10}$$

Since 1968, the solar wind eVDF outside the orbit of Mercury has been generally observed to have this reproducibly leptokurtic, nonthermal, and skewed form of Figure 3; it continues to be seen on Parker Solar Probe.

For context requested by the referee, Figure 5 provides a third semilogarithmic profile of Equation (9) using electron kinetic energy of the electrons in the ion rest frame as the independent variable. As expected from differentiable maps, this figure also shows the occurrence of a smooth transition between the dominance of f_c and f_h and that the superposition of $f_c + f_h$ does *not* produce a sharp corner at the hinge energy $\mathcal{E}_=$.

The existence of the sharp angular transition in the even Legendre terms of the eVDF (Scudder 2019b) reflects its choice of basis functions that are nonoverlapping in velocity space, rather than the superposition of components, each defined in all of velocity space used to achieve the Wind 3DP eVDF modeling seen in Figure 4 or Figure 5. The model in Scudder (2019b) only pertains to the even part of the eVDF; transport signatures are expected to produce transitions that smooth out the apparent corners, giving the entire eVDF a less angular appearance (see Figure 4 Scudder 2019b).

Large databases made over the past 50 yr (including those used for examples in this paper) are invariably well modeled with parameters that validate Equation (9)'s skewed leptokurtic form, including its 3D pitch-angle continuation (Salem et al. 2021) that reduces to the projection given by Equation (9). Recent Parker Solar Probe results appear to challenge the pervasiveness of the portions of the sunward halo component (Halekas et al. 2021), but not the existence of the leptokurtic thermal-to-nonthermal transition. Neither of the subcomponents $f_c(v)$ and $f_h(v)$ is *separately* completely constrained at all speeds by the spacecraft measurements; the observations for this $f(v)$ profile are well constrained by the composite values from the fits along and nearby the field direction, $f_e(\mathbf{v})$, including the specific ray along $\hat{\mathbf{b}}$. Recovery of unique properties of each subcomponent contributing to the eVDF value is less sure than the fit's recovery of the properties of the eVDF surface constrained by all the corrected raw counts measured by the plasma electrostatic analyzers. If the composite fit replicates the trend of the speed dependence of the data well, it suffices to infer the needed properties exploited below.

6. Maxwellians

A Maxwellian, f_{Max}, has a distinguishing geometrical property: the second derivative with respect to any Cartesian component of the velocity, v_k, of its logarithm $\ln f_{\mathrm{Max}}$ is *everywhere* the same negative constant value set by the Maxwellian's temperature:

$$\frac{d^2 \ln f_{\mathrm{Max}}(v)}{dv_k^2} = -\frac{2}{w_e^2} = -|\mathcal{C}|, \qquad (11)$$

where w_e is the rms speed of the Maxwellian associated with its temperature $2k_{\mathrm{B}}T_e = mw_e^2$.

The local mathematical curvature of a planar curve is proportional to its second derivative and has the same sign. Curves with negative curvature are concave opening downward; those with positive curvature are concave upward. A pure 1D Maxwellian implies that $\ln f(v) = a + bv - |\mathcal{C}|/2v^2$, so that its second derivative is always negative, *independent* of the value of the speed, v, of the magnetic-field-aligned Cartesian component where the curvature is evaluated.

Dreicer's (1959) insight, generalized by Fuchs et al. (1986), suggested that for any finite $E_\parallel$ there will exist a candidate runaway minimum speed v_ϖ along $-E_\parallel \hat{\mathbf{b}}$ that should occur *within the red negative curvature* domain of $f(v \gtrsim U_c)$ and thus between

$$\begin{aligned} U_c \leqslant v_\varpi &\leqslant v_I < v_= \\ \mathcal{E}_c \leqslant \mathcal{E}_\varpi &\leqslant \mathcal{E}_I < \mathcal{E}_=. \end{aligned} \qquad (12)$$

For future simplicity we identify the dimensionless energies $\mathcal{E}_q$ associated with particles at each candidate speed boundary, v_q,

where this dimensionless energy variable $\mathcal{E}_q = mv_q^2/(2kT_c)$ generalizes Dreicer's notation for $\mathcal{E}_\varpi$.

These inequalities preclude identifying v_ϖ with $v_=$ because the latter is within the blue, positive second derivative domain of $\ln f(v)$, which is separated by the inflection point v_I from *any* red negative second derivative domain for $\ln f$ at the lowest energies going toward the Sun. Since the sunward-propagating parts of all solar wind eVDFs are leptokurtic, they all possess inflection points, so any candidate runaway boundary transition from a purely Maxwellian form within $\mathbb{S}$ must occur below $v < v_I$.

7. Experimental Assay of $\mathcal{E}_\varpi$ and $|\mathbb{E}_\parallel|$

The defining property in Equation (11) for a Maxwellian suggests a natural way to process the ith spectrum for the speed variation of the velocity spread, or *dispersion*, $w_{\mathrm{eff}}^2(i, v)$. With a generally leptokurtic $f(i, v)$, this dispersion is anticipated to increase as v grows. The initial low-speed regime has a constant, nearly Maxwellian negative concavity that with increasing speed v becomes less negative, approaching zero at v_I. The remainder of this section concerns the ith spectrum; to simplify notation, the i spectrum index dependence has been suppressed.

In analogy with Equation (11), the quantity $w_{\mathrm{eff}}^2(v)$ is defined using the same second derivative operation, but now acting on the analytical fit characterization (Equation (9)) of the observed eVDF:

$$\begin{aligned} \frac{1}{w_{\mathrm{eff}}^2(v)} &\equiv -\frac{1}{2}\frac{d^2 \ln f(v)}{dv^2} \\ \mathbb{C}(v) &\equiv -\frac{w_{\mathrm{eff}}^2(U_c)}{w_{\mathrm{eff}}^2(v)}, \end{aligned} \qquad (13)$$

where the second form defines the needed dimensionless second derivative $\mathbb{C}(v)$ for the spectrum's observed $\ln f(v)$. For the composite function at $v = U_c$ the second derivative is not precisely that of the core Maxwellian because $f_h(U_c) \neq 0$. With the above procedure, however, $\mathbb{C}(U_c) = -1$ as desired. Details of the calculation of $\mathbb{C}$ and its related functions from the modeled eVDF may be found in Section A.4.

A dimensionless profile for $\mathbb{C}(\mathcal{E} \equiv E/kT_c)$ (using Figure 3) is shown as the lower black curve in Figure 6, rising from -1 at $v = U_c$; it eventually becomes 0 at the inflection point $v = v_I$. To the extent that $\mathbb{C}$ differs from -1, departures of $f(v)$ from a Maxwellian form can be quantified.

$\mathbb{T}$ is a useful variant of $\mathbb{C}$; it quantifies the speed-dependent dispersion relative to its value at $v = U_c$, giving a speed-dependent *effective* scaled temperature, $\mathbb{T}(v)$, along the profile relative to its value at $v = U_b$,
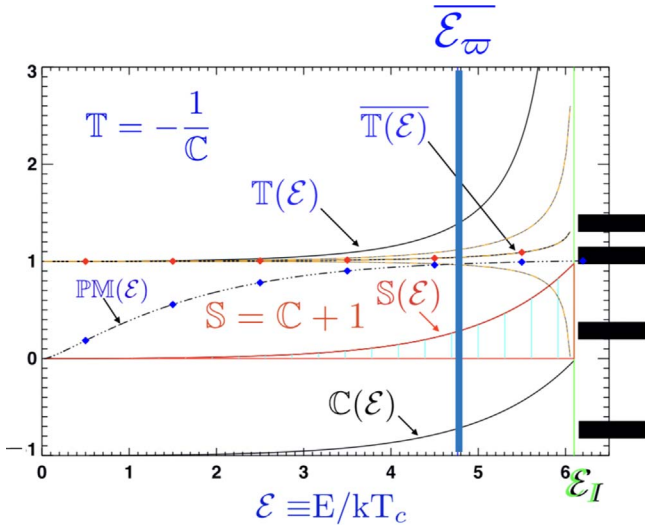
$$\mathbb{T}(\mathcal{E}) \equiv -\frac{1}{\mathbb{C}(\mathcal{E})}, \qquad (14)$$

shown as the top curve in Figure 2. It provides a sensitive indicator of the modifications to $\ln f(v)$ occurring with increasing admixtures of the halo subcomponent. Eventually its unphysical use as an effective temperature is clear when $\mathbb{T}(v \uparrow v_I) \to \infty$.

A more useful related bounded positive form is

$$\mathbb{S}(\mathcal{E}) \equiv 1 + \mathbb{C}(\mathcal{E}), \qquad (15)$$

Figure 6. The five curves in this figure illustrate the functional dependence of quantities monitored while obtaining $\mathcal{E}_\varpi$ from 4 yr of data using the Wind 3DP eVDF using Equation (16). The three curves $\mathbb{T}$, $\mathbb{S}$, $\mathbb{C}$ are pointwise dependent on the speed/energy being considered for $\mathcal{E}_\varpi$ to be Dreicer's transition. By contrast, $\overline{\mathbb{T}}(\mathcal{E})$ is an average over the pointwise variations of $\mathbb{T}(\mathcal{E}')$ for $\mathcal{E}' \leqslant \mathcal{E}$. The fifth curve outlined with black dashes and dots and dispersed blue diamonds demonstrates the limitations of the partial moment $\mathbb{PM}$ method as an alternative to Equation (16).

illustrated by the red curve in the middle of Figure 6, rising above 0, indicated by the red horizontal line. (This use of $\mathbb{S}$ should not be confused with the same symbol's use for the coulomb separatrix in Figure 2.) The height of the red curve above the red horizontal line at each energy of $\mathbb{S}(\mathcal{E})$ measures the *increase* made in $\mathbb{C}(\mathcal{E})$, as it reduces its negative size en route to 0 at $\mathcal{E}_I$, the inflection point's green vertical line. On the interval $[\mathcal{E}_{U_c}, \mathcal{E}_I]$ $\mathbb{S}$ is a positive quantity $0 \leqslant \mathbb{S}(\mathcal{E}) \leqslant 1$, with a pattern shown by the red curve in Figure 6, providing a picture of the departure of the observed $f(v)$ from a Maxwellian form $\mathbb{S} = 0$ at very low speeds to one strongly modified at $v = v_I$ with $\mathbb{S} = 1$. The blue vertical line is at the computed value of $\mathcal{E}_\varpi$ for the spectrum in Figure 3 (using Equation (16) and below), while the green vertical line indicates the energy $\mathcal{E}_I$ associated with the inflection point of the same spectrum for $\ln f$, where $\mathbb{C}(\mathcal{E}_I) = 0$, $\mathbb{S}(\mathcal{E}_I) = 1$, and $\mathbb{T}(\mathcal{E}_I) = \infty$.

The orange and black dotted curve with red diamonds superposed shows the running average $\overline{\mathbb{T}}(\mathcal{E})$ of $\mathbb{T}$ over all energies lower than that where the point is plotted. Two flaring orange curves with black dashes show the variance on this running mean. This retro-analysis shows that the running mean of $\overline{\mathbb{T}}(\mathcal{E}_\varpi)$ has departed from unity by much less than its variance until $\mathcal{E} \to \mathcal{E}_\varpi$. The routinely determined size of $\mathcal{E}_\varpi$ discussed below with the full 4 yr data set has been shown to share this property (not shown).

The growing wedge between $\mathbb{S}(\mathcal{E})$ and the horizontal axis $\mathbb{S} = 0$ enclosed by the red curve provides a way to compute *the departures of the curvature* of $\ln f(v)$ at v from that of $\ln f(v)$ at $v = U_c$. As can be seen from Figure 6, the departures do not have an edge identifiable as Dreicer's boundary minimum speed runaway boundary; nonetheless, it is possible to say in what range of energies $f(v)$ deviates strongly from an underlying Maxwellian form. We know from arguments above that $\mathcal{E}_\varpi$ must be within the interval $[\mathcal{E}_c, \mathcal{E}_I]$ and, by the variation

of $\mathbb{C}$ on this interval, must favor the location of stronger $\mathbb{S}(E)$ departures from zero that occur below, but generally near $\mathcal{E}_I$.

To find a prescription for $\mathcal{E}_\varpi$, we have considered separately the weighted averages of (1) $\mathcal{E}$ and (2) $\mathcal{E}^{-1}$ using $\mathbb{S}(\mathcal{E})$ as a weighting function. The form of the weight $\mathbb{S}(\mathcal{E})$ ensures that the selected range for $\mathcal{E}_\varpi$ emphasizes the first significant departure of $f(v)$ from a Maxwellian shape on the interval $[U_c, v_I]$. In this connection it is important to emphasize that the functional dependence of $\mathbb{S}$ is constructed from each new eVDF as a measure of the deviation of its $\ln f(v)$ curvature at v, $\mathbb{C}(v)$, from its curvature at U_c given by $\mathbb{C}(U_b)$.

8. The Recipe

This approach produces two well-defined *candidates* for the energy of Dreicer's boundary given by

$$\mathcal{E}_\varpi^{(1)} = \frac{\int_\alpha^\beta \mathbb{S}(\mathcal{E})\mathcal{E}d\mathcal{E}}{\int_\alpha^\beta \mathbb{S}(\mathcal{E})d\mathcal{E}}; \quad \mathcal{E}_\varpi^{(2)} = \left[\frac{\int_\alpha^\beta \mathbb{S}(\mathcal{E})\mathcal{E}^{-1}d\mathcal{E}}{\int_\alpha^\beta \mathbb{S}(\mathcal{E})d\mathcal{E}}\right]^{-1}, \quad (16)$$

where the common limits of integration are $\alpha = \mathcal{E}_{U_c}$ and $\beta = \mathcal{E}_I$, respectively. These two estimates have separate biases: the first toward bigger and the second toward the smaller values of $\mathcal{E}_\varpi$. These functional forms are motivated by the desire to infer $\mathbb{E}_\parallel$ that depends on $\mathcal{E}^{-1}$ and $\mathcal{E}_\varpi$ that is linear in $\mathcal{E}$.

Our approach operationally assigns the average $\overline{\mathcal{E}_\varpi}$ (indicated by the overbar) and half the difference of these estimates for further use in computations involving $\mathbb{E}_\parallel$ while retaining an idea of their ambiguity, namely,

$$\overline{\mathcal{E}_\varpi} \equiv \varpi^2 \equiv \frac{1}{2}[\mathcal{E}_\varpi^{(1)} + \mathcal{E}_\varpi^{(2)}]; \quad \sigma_{\overline{\mathcal{E}}} \simeq \frac{1}{2}|\mathcal{E}_\varpi^{(1)} - \mathcal{E}_\varpi^{(2)}|. \quad (17)$$

The dimensionless electric field and its imprecision have been inferred separately for each spectrum from

$$\overline{|\mathbb{E}_\parallel|} \equiv \frac{3}{2}[1/\mathcal{E}_\varpi^{(1)} + 1/\mathcal{E}_\varpi^{(2)}]; \quad \sigma_{\overline{|\mathbb{E}_\parallel|}} \simeq \frac{3}{2}|1/\mathcal{E}_\varpi^{(1)} - 1/\mathcal{E}_\varpi^{(2)}|. \quad (18)$$

This approach to the computed average energy $\overline{\mathcal{E}_\varpi}$ and $\overline{|\mathbb{E}_\parallel|}$ considers all the locales where $\mathbb{S}(v \leqslant v_I) \neq 0$ without specifying the lower limit of speed integration for performing the average; this is desirable since such an ab initio specification would imply knowing what sized departures in curvature of $f(v)$ in Figure 1 from that of the central region of the thermal core were or were not important. *In the above approach the fractional errors of $\overline{\mathcal{E}_\varpi}$ and $\overline{|\mathbb{E}_\parallel|}$ are algebraically equal.*

9. Overview of Properties of $\overline{|\mathbb{E}_\parallel|}$ and $\overline{E_\parallel}$

A broad overview of the derived data products is now possible. Having clearly defined how $\overline{|\mathbb{E}_\parallel|}$ is defined above, in the remainder $\mathbb{E}_\parallel$ is used.

9.1. Size Distribution and Organization of $\mathbb{E}_\parallel = \overline{|\mathbb{E}_\parallel|}$

The primary experimental observable of this new technique is the *nonnegative dimensionless scalar strength* of the parallel electric field, $\mathbb{E}_\parallel \gtrsim 0$. As $\mathbb{E}_\parallel$ is the directly observed scalar quantity of this new method, it does not require a very high angular precision determination of the total electric field $\boldsymbol{E}$ to project its parallel component along the magnetic field. The present method has sidestepped trigonometry; this is essential
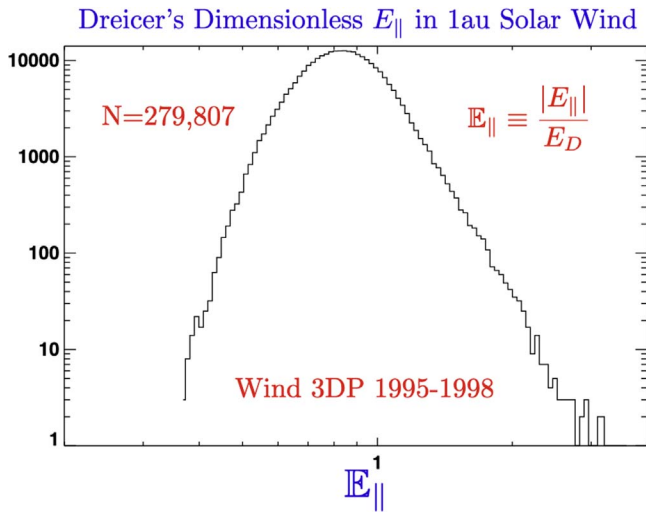
**Figure 7.** The 4 yr survey of direct measurements of Dreicer's dimensionless electric field, $\mathbb{E}_{\parallel}$, in the solar wind determined using a new technique developed of this paper demonstrating that $\mathbb{E}_{\parallel}$ at temporal cadence of 96 s is ubiquitously strong at 1 au using all 279,807 readings obtained over 4 yr between 1995 and 1998.

Figure 8. Common logarithm of the column-normalized (COLN) probability of occurrence of the dimensionless $|\mathbb{E}_{\parallel}(r_{\oplus}, U)|$ vs. solar wind speed $U(r_{\oplus})$ showing positive correlation at 1 au.

given the expected very small size of the wind's ambipolar $E_{\parallel} \simeq 0.1$ nV m^{-1}, which is 10 million times smaller than 1 au MHD unipolar $|\boldsymbol{E}_{\perp}|$ fields of $\simeq \mathcal{O}(2$ mV m$^{-1})$.

Figure 7 provides an inventory of all the *observed occurrences* of $\mathbb{E}_{\parallel}$ at the forward Lagrangian point during the interval of 1995–1998 with bulk speeds ranging between 265 and 800 km s^{-1}. Its shape, mode, and mean depend on the mixture of readings presented by the controlling factors of wind states diagnosed during the 4 yr interval.

Unequivocally the detected $\mathbb{E}_{\parallel}$ at 1 au ranged between 0.25 and 3.1. By extension $E_{\parallel}$ in the solar wind at 1 au is demonstrated with these measurements to be *strong*, since all exceed the upper threshold of $\mathbb{E}_{\parallel} > 0.05$ where a parallel electric field is known to be weak (see Scudder & Karimabdi 2013 and references there). The observed range reported here is consistent with anecdotal observations or inferences using radial pressure power-law estimates to infer spatial gradients (Scudder 1996; Issautier et al. 1998; Scudder 2019a) and arguments from modeling (Lemaire & Scherer 1971; Landi & Pantelinni 2003; Meyer-Vernet 2007; Scudder & Karimabdi 2013; Scudder 2019c).

The two-dimensional histogram of Figure 8 helps to give a clearer picture of the 4 yr statistics of the *probability of occurrence* of $\mathbb{E}_{\parallel}(U)$ versus ambient wind speed U. This format will be used several times in this paper: the data are binned in two dimensions, with the number of observations in the *i*th row of the *j*th column normalized by the peak number of observations in the *j*th column. When this normalization has occurred, the annotation COLN is placed in the lower left corner. The color code in a given pixel is set by the logarithm $\mathcal{P}$ of the probability of occurrence relative to its column maximum. The logarithm of the probability $\mathcal{P}$ decreases from yellow according to the color bar, with increasingly darker colors used for decreasing values. Blue diamonds denote column averages of the observed row values in the column and are often connected to suggest their variation with bulk speed (abscissa). All points of equal normalized probability across ordinate and abscissa are circumscribed by the cyan contour at the one *e*-folding level of $\text{Log}_{10}(e^{-1})$. The coordinates of
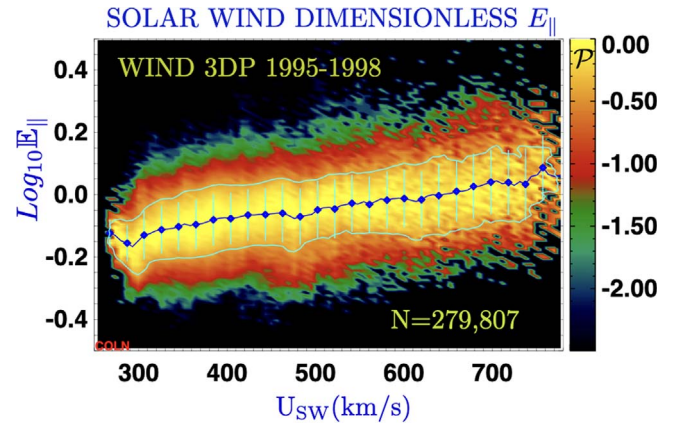
the interior of this contour define the 2D space of high relative probability of occurrence, devoid of the overcounting that occurs for bins by just counting the number of observations across the grid.

In this figure the bulk speed is binned along the *x*-axis and the common logarithm of $\mathbb{E}_{\parallel}$ along *y*. The blue curve connecting diamonds illustrates a steady but weak exponential growth of $\mathbb{E}_{\parallel}$ as the wind speed increases between 275 and 750 km s^{-1} as anticipated in Figure 1 of Scudder (2019b). The substantial yellow width $\Delta \mathbb{E}_{\parallel}$ of this colored 2D histogram, or equivalently of the cyan contour, suggests that the bulk speed is not the only predictor of the recorded size of $\mathbb{E}_{\parallel}$.

However, the cyan contour in Figure 8 shows at the highest normalized probability across sampled solar wind speeds that $\mathbb{E}_{\parallel} = \mathcal{O}(1)$ is routinely large and increasing across a wide range of wind speeds. This finding is consistent with anecdotal inferences using power-law radial profile estimates to estimate spatial gradients (Scudder 1996, 2019a, 2019c; Issautier et al. 1998; Halekas et al. 2020, and Maksimović et al. 2020).

The new measurements presented in Figure 8 are strong support for the SERM thesis (Scudder 2019b), since such recurrently strong $\mathbb{E}_{\parallel}$ contradict the central tenets of various transport efforts that presume a *perturbatively weak* $\mathbb{E}_{\parallel} < 0.05$ (Scudder 2019c) and attempt to explain transport in that medium with perturbative modifications to local Maxwellians. SERM suggested that strong $\mathbb{E}_{\parallel}$ conditions were the cause of the puzzling ubiquity of the leptokurtic electron eVDFs (Scudder 2019b). The generically required and now measured $\mathbb{E}_{\parallel} \simeq \mathcal{O}(1)$ of the wind insists that its physics cannot be recovered starting from local Maxwellian eVDFs that have always been predicated on perturbatively small $\mathbb{E}_{\parallel}$.

9.2. Polarity/Size Distribution and Organization of $E_{\parallel}$

The signed value of $E_{\parallel}$ and its radial projection E_r (often reported from exospheric solutions) are set by definitions, using the observed nonnegative 3DP scalar $\mathbb{E}_{\parallel}$, and Equation (5) to determine the signed vector

$$\boldsymbol{E}_{\parallel} \equiv E_{\parallel}\hat{\boldsymbol{b}} = \hat{\boldsymbol{b}}\frac{q_{\parallel}}{|q_{\parallel}|}E_D \overline{|\mathbb{E}_{\parallel}|} \qquad (19)$$

without trigonometry. Thus, $E_{\parallel}$ is fully determined after consulting concurrent determinations of the scalars $\mathbb{E}_{\parallel}$, $E_D(n_e, T_e)$ together with measured values of the signed parallel

Size Ambipolar Parallel E at 1au
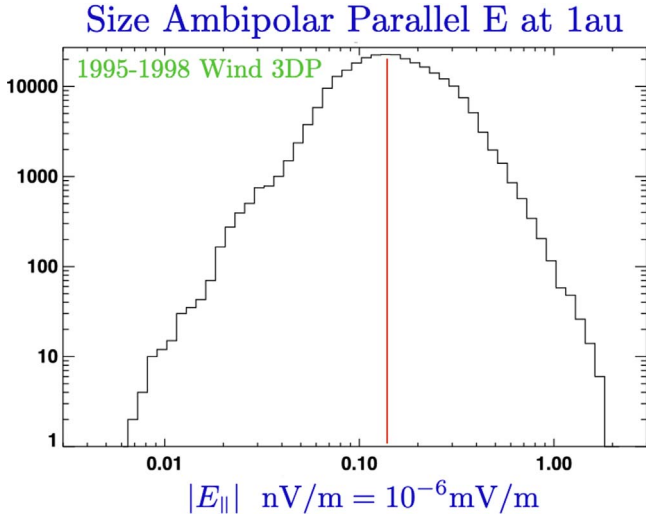
Figure 9. Nearly lognormal distribution of $|E_\parallel|$ in nV m^{-1} with modal size approximately 0.12 nV m^{-1}, but ranging between 0.007 and 1.9 nV m^{-1} on rare occasions. Such determinations are more than 10 million times weaker than the unipolar electric field that moves charged particles across field lines at 1 au.

electron heat flux $\hat{b} \cdot q_e$. Trigonometry only enters when solving for the equivalent radial electrostatic field: $E_r = E_\parallel / \hat{b} \cdot \hat{r}$.

The most probable size of $E_\parallel$ determined by Wind 3DP observations is of the order of 0.12 nV m^{-1}, as shown in the histogram of all measurements of $|E_\parallel|$ depicted in Figure 9.

The variation of the normalized probability for observing $|E_\parallel|(U)$ with Wind solar wind speed, U, is shown in Figure 10; for uniformity of interpretation this figure has been made of Log$_{10}|E_\parallel$ nV m$^{-1}|$ versus U(km s^{-1}) from observations selected by $E_r(U) > 0$ in a semilogarithmic 2D histogram format.

Generally $|E_\parallel|$ is a *decreasing* function of *increasing* solar wind speed; a similar pattern is observed (but not shown) restricting the data to either $E_r < 0$ or $E_r > 0$.

By contrast, the bulk speed dependence of $\mathbb{E}_\parallel(U)$ shown above is nearly *linear* and *rising* in the semilogarithmic form of Figure 8, despite their common semilogarithmic formats.

Since the steady-state solar wind is associated with

$$E_r \equiv \frac{E_\parallel}{\hat{b} \cdot \hat{r}} > 0, \qquad (20)$$

the measured sign distributions of $E_\parallel$ and E_r from it are of supporting interest to the validity of the observations. The observed signs of $E_\parallel$ shown in Figure 11 are nearly equally represented (44%–56%), while the distributions of their radial projections, E_r, are biased more than 3:1 in favor of the positive sense: 76% versus 24%. Positive E_r would correspond, for example, to the sense expected for the USSSW expectations. An outward magnetic sector in spherical coordinates has $\hat{b} \cdot \hat{r} < 1$; for such conditions $E_\parallel < 0$ is expected to correspond to $E_r > 0$, producing a force on electrons that is toward the Sun along $\hat{b}$. For an inward sector $E_r > 0$ requires $E_\parallel > 0$.

Because the method that extracts signed $E_\parallel$ uses the 3DP electron heat flow sense along $\hat{b}$, the preference of E_r to be positive is essentially the same frequency as for the radial component of $q_\parallel$ being outward for the radial expansion. However, as is well known, on the 96 s spectrum resolution

SOLAR WIND PARALLEL ELECTRIC FIELD
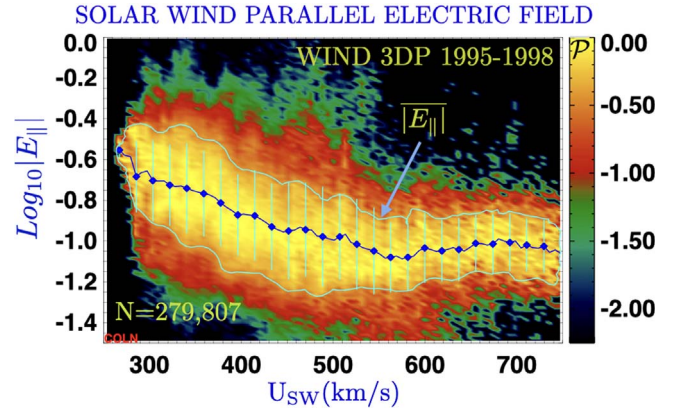
Figure 10. Bulk speed organization of probability of detection implied by Wind-SERM observations of Log$|E_\parallel$(nV m^{-1})$|(U)$. The superposed blue connect-the-dot curve joins the 80 vertical column averages. This curve (with column variances indicated by the cyan flags) shows the bulk speed trend of the column mean. For reference the cyan contour is the locus of probability e^{-1} throughout the 2D histogram.

SERM's Ambipolar E$_\parallel$ from eVDF
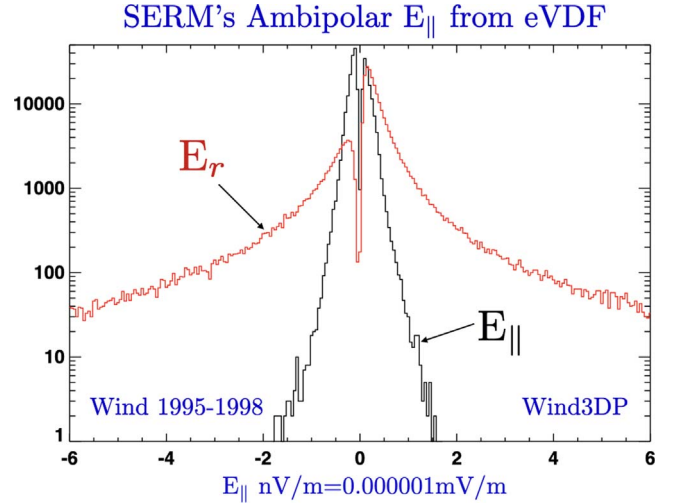
Figure 11. The 4 yr distributions of $E_\parallel$ (indicated in black) and the radial component of this parallel electric field E_r (in red) segregated by polarity relative to $\hat{b}$ and $\hat{r}$.

flux tubes can locally be oriented so as to take coronal heat flux toward the Sun when the radial coordinate of a field line does not locally grow monotonically with arc length.

9.3. Reliability of Wind $E_\parallel$ Determinations

For future use the precision and accuracy of the present method's determination of parallel electric fields are needed: (i) the *precision* of the determination is related to the reproducibility of the numeric value reported; by contrast, (ii) the *accuracy* seeks to quantify the calibration of these reproducible numbers, to show that these numbers are corroborated as the physical quantity identified by the observer to be the cause of the values reported.

9.3.1. Precision of $\mathbb{E}_\parallel$ and $E_\parallel$

The probability distribution of the fractional spread $\sigma_{\overline{\mathbb{E}_\parallel}}/\overline{|\mathbb{E}_\parallel|}$ shown in Figure 12 gives a statistical inventory of the computed *reproducibility precision* of $\overline{\mathbb{E}_\parallel}$. Using all observations across the 4 yr of this study, the histogram shows a
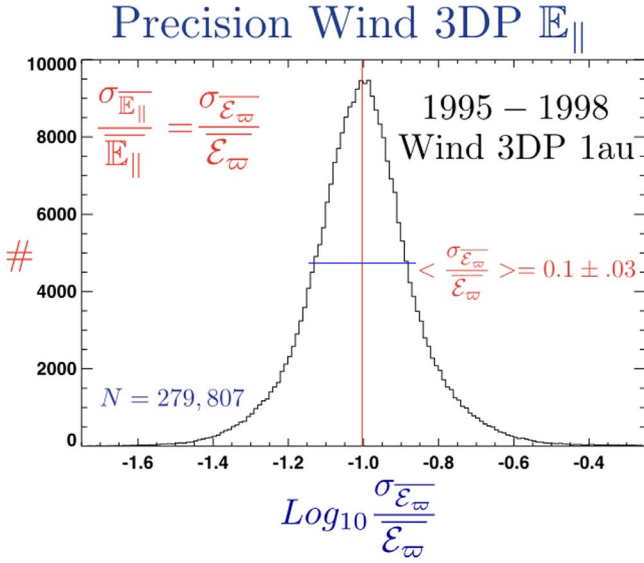
Figure 12. Histogram showing the average precision of the Wind determination of $\mathbb{E}_\parallel$ to be 10% using two separate estimates for each data determination via Equation (16).

lognormal distribution of the estimated fractional *precision* of the $\overline{\mathbb{E}_\parallel}$, with a mean value of 0.1 ± 0.03.

It must be emphasized that the values used for Figure 12 come from evaluating two different formulations (given in Equation (16)) that have slightly different systematic defects. By construction, their comparison determines a *numerical measure* of the reproducibility of $\overline{\mathbb{E}_\parallel}$ for each 96 s spectrum; it is not an off-hand, possibly inaccurate, *ad hoc surmise* of this attribute.

Exceptional reproducibility *could* be the result of dominating systematic error; to guard against this, the complementary tests for accuracy are needed. Throughout the discussion below the reproducibility error of this type is carried with each estimate of $\overline{\mathbb{E}_\parallel}$. It is known but not shown that this error is systematically, but only slightly, smaller in the slow wind rather than in the faster wind, with the 10% estimate a compromise between these two extremes, and its variance is an overstatement of the typical variation of that precision in any given localized speed domain.

The accuracy and reproducibility of $E_\parallel$ are essentially that for $\mathbb{E}_\parallel$, provided that the sense of the measured skewness of the eVDF is not in question. Using Equation (19) and E_D's definition argues that the reproducibility of $E_\parallel$ is essentially synonymous with that for $\mathbb{E}_\parallel$; the accuracy of $E_\parallel$ is degraded by the fractional accuracy of n_e, T_e,

$$\frac{\delta E_\parallel}{E_\parallel} \simeq \sqrt{\left(\frac{\delta \mathbb{E}_\parallel}{\mathbb{E}_\parallel}\right)^2 + \left(\frac{\delta n_e}{n_e}\right)^2 + \left(\frac{\delta T_e}{T_e}\right)^2}. \quad (21)$$

Given the effort to constrain the 3DP moment evaluations by cross-strapping them with those of the plasma line documented in Salem et al. (2003, 2021), the uncertainties of $\mathbb{E}_\parallel$ overpower those residual fractional errors arising from unpacking the direct $\mathbb{E}_\parallel$ measurement.

9.3.2. Accuracy of Wind $E_\parallel$ Determinations

The experimental results of the above program will now be inventoried for their *accuracy* in two different ways: (i) assume that the electric field determinations are independent of other simultaneous plasma and magnetic field observations, and contrast the size of the electric fields with estimates theoretically expected to be similar using simultaneously measured Wind 3DP moment data properties and *the externally supplied radial gradients needed*. An alternate approach for an accuracy test is to (ii) proceed by *reductio ad absurdum*: suppose that the electric field measurements and all colocated Wind 3DP electron moments are accurate and use the approximate electron momentum equation to determine the required electron pressure gradients that fulfill the force balance. Contrasting these *computed* bulk-speed-dependent gradients with recently published estimates of these gradients from power-law fits to radial pressure profile should allow an assessment of possible inconsistencies or confirmation of the *accuracy* of $E_\parallel$ determinations reported here.

10. The Program for an Inventory of Wind $E_\parallel$ Accuracy

Allowing for pressure anisotropy $\mathcal{A}_e \equiv P_{e\parallel}/P_{e\perp}$, the leading-order terms in the generalized Ohm's law simplify for a gyrotropic electron pressure tensor $\mathbb{P}_e$ to give an explicit plasma recipe that should approximate the dimensionless $\mathbb{E}_\parallel$:

$$|\mathbb{E}_\parallel| \simeq \frac{|\mathbb{K}_{P_e}|}{2} \equiv \frac{3\lambda_{\mathrm{mfp}}|\hat{\boldsymbol{b}} \cdot \nabla \cdot \mathbb{P}_e|}{2\,\mathrm{Tr}\,\mathbb{P}_e} \equiv \frac{\lambda_{\mathrm{mfp}}}{2\mathcal{L}_\parallel}$$

$$\frac{1}{\mathcal{L}_\parallel} = \frac{3T_{e\parallel}}{rT_e} \left| \left[\epsilon_{P_{e\parallel r}} + \frac{1 - \mathcal{A}_e}{\mathcal{A}_e} \epsilon_{Br} \right] \hat{\boldsymbol{b}} \cdot \hat{\boldsymbol{r}} \right|, \quad (22)$$

where Equation (A4) has been used and a pressure Knudsen number $\mathbb{K}_{P_e}$ introduced. Equation (22) specifies the relevant length scale $\mathcal{L}_\parallel$ for the sense in which this plasma recipe for $\mathbb{E}_\parallel$ is synonymous with *half the mean free path for coulomb scattering divided by a scale length along the magnetic field*.

The quantities $\epsilon_{\chi,r}$ may be thought of as the (negative or inverse of the) local radial power-law exponent of χ at r:
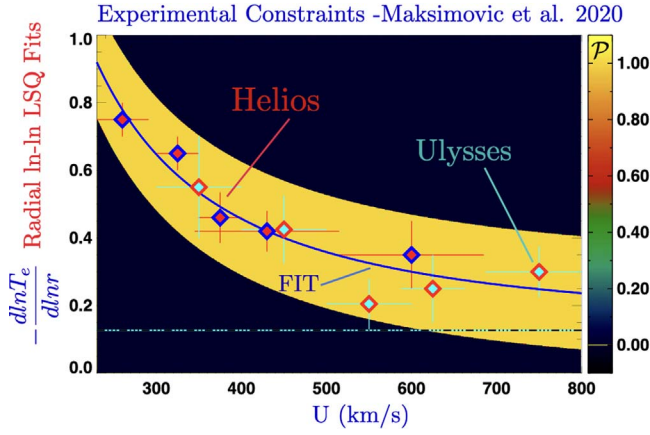
$$\epsilon_{\chi_r} = -\frac{d\ln\chi}{d\ln r}. \quad (23)$$

The sign of ϵ_{χ_r} is positive when χ decreases with increasing r (as with *most* spherically symmetric wind profiles) and negative when increasing with increasing r.

Since $\mathcal{L}_\parallel$ is determined by ϵ_{χ_r}, $\mathcal{A}_e$, and T_e, it is not a strong function of the solar wind bulk speed. Apparently the bulk speed variation of $\mathbb{E}_\parallel$ is controlled by that of λ_{mfp}; it in turn is dominated by the inverse density dependence with only weak input from $T_e(U)$. The tendency for mass conservation at 1 au then implies that $\mathbb{E}_\parallel(U)$ should be an increasing function of bulk speed with a slope that depends on magnetic geometries. The general behavior of $\mathbb{E}_\parallel(U)$ in Figure 8 may have this as its explanation.

After exploiting the definition of $\mathbb{E}_\parallel$, Equation (22) provides the theoretical expectation, $\Gamma_\parallel$ *using only plasma variables* for the *signed* parallel electric field at 1 au:

$$E_\parallel \simeq \Gamma_\parallel \equiv \frac{k_B T_{e\parallel}}{er_\oplus} \left[\epsilon_{P_{e\parallel r}} + \frac{1 - \mathcal{A}_e}{\mathcal{A}_e} \epsilon_{|B|r} \right] \hat{\boldsymbol{b}} \cdot \hat{\boldsymbol{r}}$$

$$E_r \simeq \Gamma_r \equiv \frac{k_B T_{e\parallel}}{er_\oplus} \left[\epsilon_{P_{er}} + \frac{1 - \mathcal{A}_e}{\mathcal{A}_e} \epsilon_{|B|r} \right], \quad (24)$$

Figure 13. Empirical variations of $\epsilon_{Te}(U)$ reported from Helios and Ulysses (crosses) vs. solar wind speed U, with the blue curve showing the fitted expression in Equation (27). The yellow band embraces essentially all error bars reported (Maksimović et al. 2020) about the modeled profile.

where $E_r \equiv E_\parallel / (\hat{\boldsymbol{b}} \cdot \hat{\boldsymbol{r}})$ is the required and larger radial electrostatic field usually reported from exospheric models: $|E_r| \gtrsim |E_\parallel|$.

Symbolically the first type of corroborations of the accuracy of Wind parallel electric field determinations involves contrasting balances of the form

$$\mathbb{E}_\parallel \simeq |\mathbb{K}_{P_e}|^* / 2$$
$$E_\parallel \simeq \Gamma_\parallel^*, \tag{25}$$

with independent measurements for each spectrum used on the two sides of this expression and needed gradients *approximated* (*) by necessary but previously known solar wind observations. Notationally the asterisk superscript reminds the reader that *gradient* approximations have been made.

The second approach tests accuracy via the *reduction ad absurdum* method: assume that the signed parallel electric field and the *structure* of Equation (25) are theoretically complete for this purpose. Under this assumption, the dominant (unmeasured) gradients may be computed by enforcing the equality of the theoretical equations. However, the single-point gradients computed in this way rely on the accuracy of all experimental inputs for $E_\parallel$, T_e, and its anisotropy $\mathcal{A}_e$. The assay of the total integrity of this accuracy comparison at 1 au rests on verifying the hypothesis that the inferred ϵ_{χ_r} are consistent with the recently published information about gradients of electron thermal properties as a function of solar wind speed (e.g., Maksimović et al. 2020) and the theoretical work that explained their occurrence (Meyer-Vernet & Issautier 1998).

Both techniques use empirical inventories of electron gradients: approach (i) *presumes* they are *adequate* for all data used; method (ii) will be shown to be able to *recover* previously reported profiles $\epsilon_{P_e r}$ when it operates on a *specific subset of the Wind data* characterized by scales known to allow for USSSW solutions (see Figures 18–20).

En route it is shown that there are other pressure gradients in the 4 yr Wind data set that are *not* compatible with the relatively recent determinations of wind gradients inferred by fitting power-law profiles to radially accumulated data sets (e.g., Halekas et al. 2020; Maksimović et al. 2020). Structures with gradient scales as small as 0.01 au with negative *and* positive power-law exponents are documented to occur in the
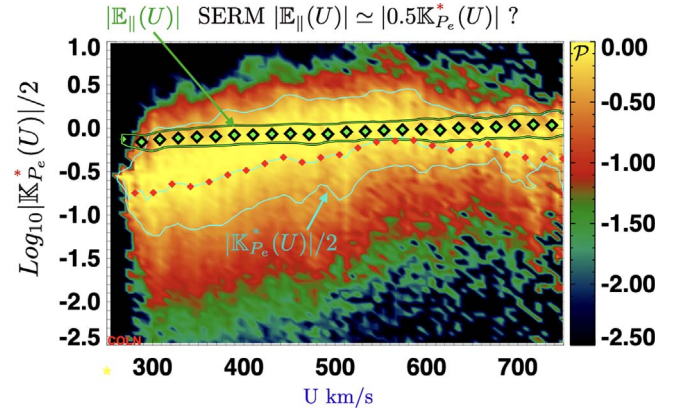
Figure 14. Superposed epoch 2D histogram of the 4 yr column-normalized probability for observing $\mathbb{K}_{P_e\parallel}^*(U)/2$. Red symbols connected by the cyan curve join the adjacent column mean values of $\mathbb{K}_{P_e\parallel}^*(U)/2$. The cyan contour curve encloses *crown e^{-1}* down from the peak probability across the entire $\mathbb{K}_{P_e\parallel}^*(U)/2$ surface. The green diamonds with black diamond inlays show the superposed epoch variation of $\mathbb{E}_\parallel(U)$ using Wind 3DP data transferred from the blue dots in Figure 8. The green contour curve reflects the *e*-folding area of $\mathbb{E}_\parallel$ as already shown in Figure 8. Close inspection shows that *almost all* $\mathbb{E}_\parallel$ diamonds and their error bars are within the *e*-folding cyan curve for $\mathbb{K}_{P_e\parallel}^*/2$.
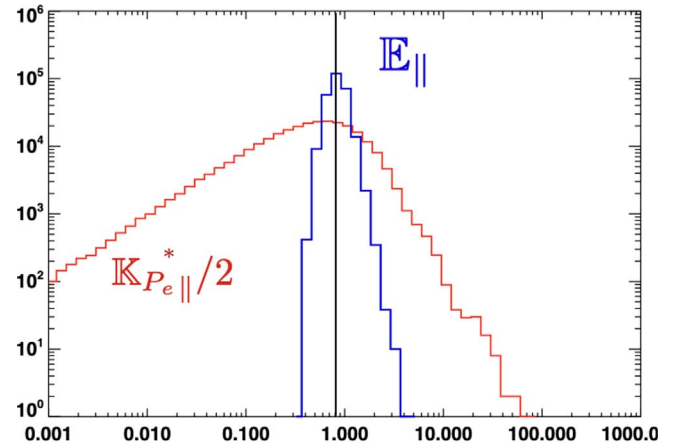

Figure 15. Comparison of 4 yr probabilities of $\mathbb{E}_\parallel$ (blue) and $|\mathbb{K}_{P_e}|^*/2$ (red). While widths are different for reasons discussed in text, the nearly perfect alignment of the modes suggests that the circumstances for which ϵ_X were adapted dominate the observations reported here, and that the measured $\mathbb{E}_\parallel$ are consistent with expectations and the size suggested by the rhs of Equation (22).

Wind data set and are outside the set of USSSW solutions having scales $\mathcal{O}(1)$ au. Short-scale pressure ridges with negative local radial power-law exponents are also commonly seen in the Wind data set.

These short-scale pressure gradient structures complicate the accuracy of Wind data comparisons shown with method (i) (in Figures 14 and 16 below). Filtering such short-scale structures out of the data set permits a proper documentation of $\mathbb{E}_\parallel$ accuracy by showing for a subset of Wind measurements (ii) that the measured $E_\parallel$ can determine the *best* known bulk speed tabulation of electron pressure and temperature gradients that are also consistent with published bulk speed dependence of electron T_e gradients determined by least-squares fits to power laws previously published.

External Gradients as a Function of Bulk Speed: Evaluating the expanded form of $\mathbb{K}_{P_e}$ in Equations (22) and (24) requires *empirical knowledge* of the coefficients $\epsilon_{X\parallel}^*$, including gradients
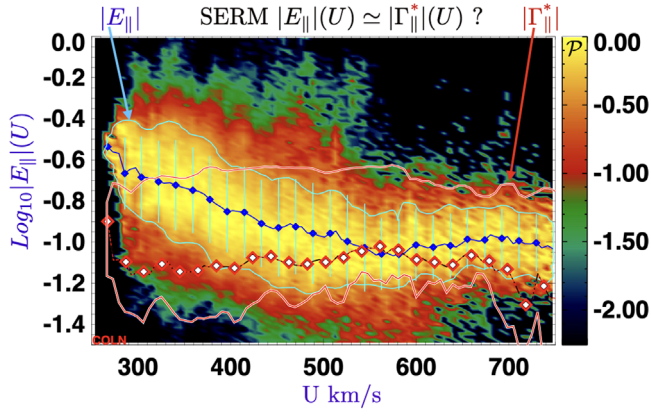
Figure 16. Blue diamonds are U bin averages for $|E_\parallel|$ enclosed by cyan e-folding contour. Red diamonds are the bin averages for $|\Gamma_\parallel^*|$ enveloped in its white–red–blue e-folding contour. Blue electric field points are mostly within the $\Gamma_\parallel^*$ crown, but at low speeds they disagree. At low speeds plasma of Knudsen-based estimate mean values is outside the $|E_\parallel|$ high-probability crown.
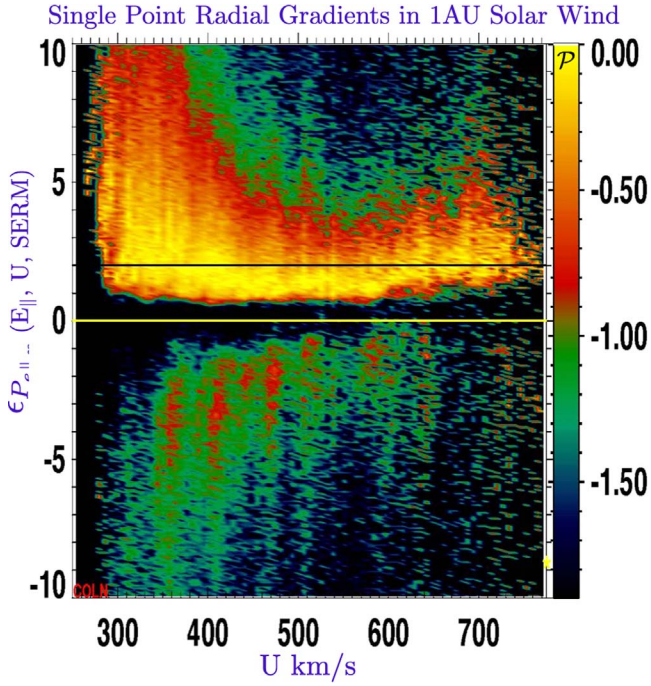

Figure 17. Visualization of the column-normalized probability of occurrence of inverse pressure gradient *exponents* $\epsilon_{P_{e\parallel}}(U)$ from which scale lengths $\mathcal{L}(U) \simeq 1\,\mathrm{au}/\epsilon_{P_{e\parallel}}$ as a function of solar wind speed U may be estimated. Most frequently occurring estimates at all wind speeds are at or just above $\epsilon_{P_{e\parallel_r}}(U) \simeq 2$, indicated in bright yellow. Yellow line: corresponds to flat pressure profiles with infinite radial scales, not a location that would typify a spherically symmetric solar wind sample. Black line: at $\epsilon_{P_{e\parallel_r}}(U) = 2$, a nearly isothermal spherically symmetric wind at its asymptotic speed would be identified. *All unstructured spherically symmetric solar wind (USSSW) profiles should possess* $2 \leqslant \epsilon_{P_{e\parallel_r}}(U) < \simeq 4$, *making* $\simeq 4 < |\epsilon_{P_{e\parallel}}|$ *and* $\epsilon_{P_{e\parallel_r}} \leqslant 0$ observations inconsistent with USSSW.

of the magnetic field strength that enter when the electrons become anisotropic.

To establish *expectations only* for the likely local size of $E_\parallel$ and $\mathbb{E}_\parallel$, we have estimated $\epsilon_{T_{er}}$ from a recent data collection of the bulk speed variation of $\epsilon_{T_{er}}(\overline{U})$ shown in Figure 13; each estimate shown was determined from radial power-law fits to $T_e(r)$ using Helios, Voyager, Ulysses, and Parker Solar Probe
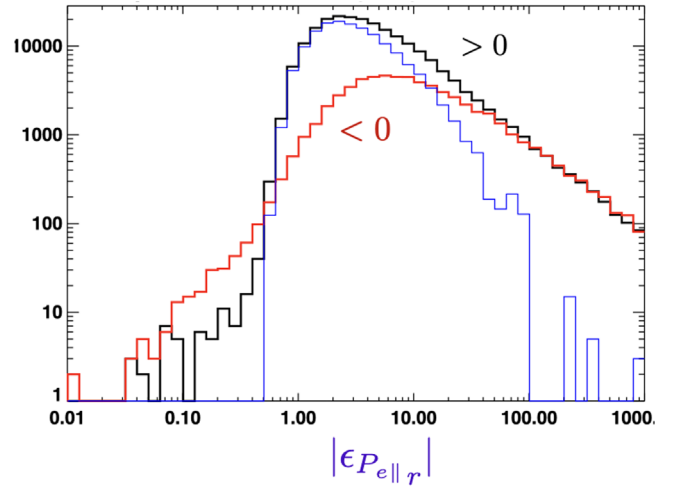
Figure 18. Cumulative histograms over all solar wind speeds of occurrence of P_e exponents seen in Figure 17 after first segregating by sign. Note the very high preference (in black (all), blue (restricted)) for positive exponents with mode just above 2. See text for fuller discussion.
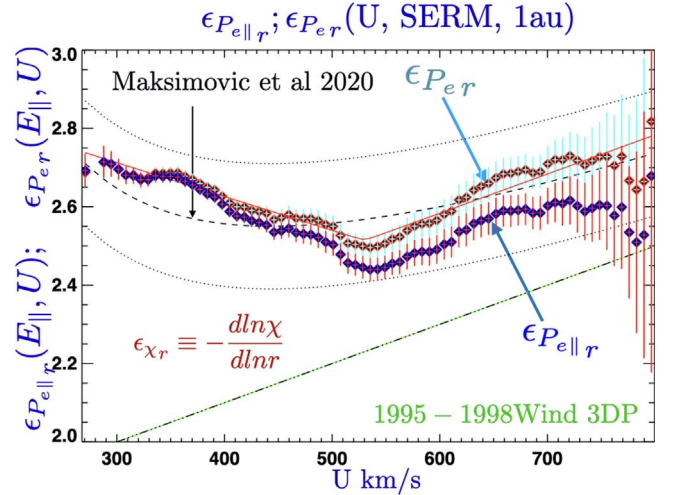

Figure 19. Blacked dotted region: expectation for $\epsilon_{P_e r}$ from measured power-law T_e profiles collated in Maksimović et al. (2020); mean trend shown by the dashed black curve. Blue diamonds with red error bars reflect the size of $\epsilon_{P_{e\parallel_r}}$ using SERM-motivated $E_\parallel$ developed in this paper. Red diamonds with cyan error bars reflect *the larger* total pressure gradients using Equation (38), $\epsilon_{P_e r}$, based on the SERM-motivated $E_\parallel$. The red curve is the expected bulk speed dependence of the total pressure based on the fit in Figure 20. The green ramp with black dashes superposed indicates the estimated contribution total pressure gradient including the residual acceleration of the wind beyond 1 au, implied by the height of the triangular ramp above horizontal at the bottom of the graph.

data (Maksimović et al. 2020). These data have been modeled in this paper by fitting them with the ad hoc form

$$\epsilon_{T_{er}}(U) \simeq 0.13 + 0.27(450\,\mathrm{km\,s^{-1}}/U)^{1.6} \qquad (26)$$

shown by the blue curve in Figure 13; the yellow region in this figure bounds all reported error bars of these power-law estimates by fits and is used for comparisons in the *reductio ad absurdum* approach for accuracy below, and as a proxy when needed for quantities like $\mathbb{K}^*_{P_e}$ of Γ^* below.

The additional relations needed at 1 au to determine the *expectations* for the radial power-law exponents of the P_e
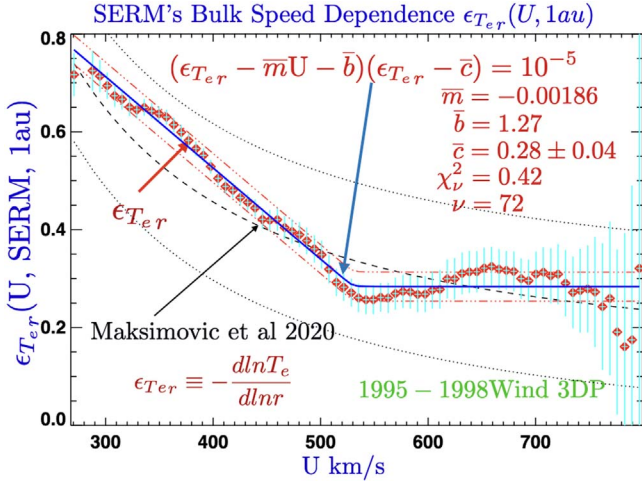
Figure 20. Red diamonds: inferred electron total temperature exponents $\epsilon_{T_e r}$ derived from single-point 1 au measurements of $E_\parallel$ determined in this paper. The solid blue curve illustrates best model fit functional form (as indicated) for the bulk speed dependence of these 76 measured single-point gradients. The parallel red dotted curve illustrates the rms departure of the data points from this curve. The black dashed curve is the earlier described radial power-law modeling of Helios and Parker Solar Probe data presented by Maksimović et al. (2020) in Figure 13; dotted flanking black curves depict the envelope of these sparse prior characterizations of radially traversed electron temperature profiles.

profile have the forms

$$\epsilon_{P_e r} \simeq \epsilon_{T_e r} + \epsilon_{nr}$$
$$\epsilon_{nr}(U) \equiv 2 + 0.001(U\,(\mathrm{km\,s^{-1}}) - 300), \qquad (27)$$

where the indicated empirical summary of bulk speed dependence at 1 au of ϵ_{nr} is determined from Helios data analysis.

As shown in Equation (24), $\epsilon_{|B|_r}$ is also required. The Parker spiral form for the magnetic field determines this bulk-speed-dependent variation at 1 au:

$$\epsilon_{|B|_r} \equiv 2 + \frac{[-1 + \epsilon_{U_r}(U)]\Omega^2 r_\oplus^2}{U^2 + \Omega^2 r_\oplus^2}. \qquad (28)$$

The recent T_e gradient summaries of Figure 13 model the observed solar wind variation as a *single* radial power law using data intervals of $\mathcal{O}(0.5)$ au, assuming spherically symmetric wind profiles with temperature scale lengths of $\mathcal{L} \simeq 1\,\mathrm{au}/\epsilon_{T_e r} > 1$ au. By the simplicity of the model such fits suppress structures in the wind that do not occur with scales comparable to or below the radial scale transited. For the entire 4 yr Wind data set a wide variety of dynamical situations are encountered so that this idealized expectation is almost certainly not generally true for every 96 s Wind data point that only contains information integrated over a length at $400\,\mathrm{km\,s^{-1}}$ in the plasma 0.00027 au long. This fact shows that the spatial minutiae in the Wind data set is richer than can possibly be inventoried by the radial profile fitting approach to data that typically span 0.5 au or more. The Wind results include steeper gradients than allowed by pressure gradient fits to such radially distended profiles (see Figure 17).

11. Accuracy Verification: Type Ia

The *observed* time variability of

$$\frac{1}{2}\mathbb{K}_{P_e}^*(T_e(t), n_e(t), \mathcal{A}_e(t), \epsilon_\chi^*(U(t)), \hat{\boldsymbol{b}}(t) \cdot \hat{\boldsymbol{r}}) \qquad (29)$$

produced by over a quarter million observations is allowed to determine a 2D histogram overview in Figure 14 for $|\mathbb{K}_{P_e}^*(U)|/2$ versus U. The closed cyan contour superposed on the colored histogram encloses the *crown* (1 e-folding down) of this Knudsen probability surface, providing a visual idea of the locales across bulk speeds of highest column-normalized probability. The red diamonds joined by a cyan curve connect the peak probabilities determined in each speed column across bulk speed columns. Additionally a picture of the *crown* of the $\mathbb{E}_\parallel(U)$ surface (shown in Figure 8) is rescaled to the present histogram's vertical scale (Figure 14) and indicated by the tight green closed contour, surrounding its maximum probability region. Green (unconnected) diamonds within the crown show the locus of peak probability for $\mathbb{E}_\parallel$ across U using the same data for the newly dimensionless electric field.

Although the loci of peaks for $|\mathbb{K}_{P_e}^*|/2$ and $\mathbb{E}_\parallel$ do not lie precisely on top of one another, the 4 yr *crown* of $\mathbb{E}_\parallel$ data does lie within the *crown* made describing the high points of the surface for $|\mathbb{K}_{P_e}^*|/2$.

This overlay shows that there are places in the frequently encountered $|\mathbb{K}_{P_e}^*|/2(U)|$ that are commensurate with mean values of $\mathbb{E}_\parallel(U)$ (except at low speeds, to which we return below). The red mean values for $|\mathbb{K}_{P_e}^*(U)|/2$ are more closely near those for $\mathbb{E}_\parallel(U)$ at higher bulk speeds than lower ones. The bare minimum conclusion is that $|\mathbb{K}_{P_e}^*(U)|/2$ is not precisely $|\mathbb{E}_\parallel(U)|$ when inventorying the entire 4 yr solar wind data set and simultaneously *assuming** that every spectrum occurred with typical solar wind gradients* that suppose USSSW conditions.

While the 2D histogram for $|\mathbb{K}_{P_e}^*(U)|/2$ in Figure 14 has a much broader vertical spread than $\mathbb{E}_\parallel(U)$ (see Figure 8), the reduced histogram in Figure 15 for all estimates of $|\mathbb{K}_{P_e}^*|/2$ (red) (regardless of U) has a most frequently occurring value very nearly that for $\mathbb{E}_\parallel(U)$ shown in blue.

Despite its augmented half-width, the mode of $\mathbb{K}_{P_e\parallel}^*/2$ is essentially synonymous with the mode for the blue $\mathbb{E}_\parallel$ histogram. Given $|\mathbb{K}_{P_e}^*|$'s disparate sensitivity to underlying suspicious assumptions* about gradient scales, the lineup of their respective modes suggests that these two quantities are most frequently of similar sizes, but again that they are not so for all readings.

12. Accuracy Verification: Type Ib

The dimensional form of the generalized Ohm's law of Equation (30) relates the signed parallel electric field to gradients in a way that makes the bulk speed trend of $E_\parallel$ in Figure 16 very suggestive:

$$E_\parallel \simeq \Gamma_\parallel^*$$
$$\equiv \frac{kT_e}{er}[\epsilon_{P_{e\parallel},r} - (1 - \mathcal{A}_e^{-1})\epsilon_{B\,r}]\hat{\boldsymbol{b}} \cdot \hat{\boldsymbol{r}}. \qquad (30)$$

Given the *observed* weak bulk speed dependence of $T_e(U)$ and $\hat{\boldsymbol{b}} \cdot \hat{\boldsymbol{r}}$, the variation of $E_\parallel(U)$ shown in Figure 16 is likely a direct reflection of the bulk speed organization of the gradients represented by the $\epsilon_{\chi\parallel}$. As indicated in Figure 13, the expected radial profile for $\epsilon_{P_e r}(U)$ will show an increase below $400\,\mathrm{km\,s^{-1}}$, as this comparison suggests would be required to balance $E_\parallel \simeq \Gamma_\parallel$ in Equation (27). While this hint has merit, this is just part of this evolving puzzle.

The variation of the Wind 3DP determinations for the columnar means of $|E_\parallel(U)|$ is reproduced in Figure 16 for the purpose of superposing the 2D histogram's *surface properties* for $\Gamma_\parallel^*$. The connected blue diamonds are the column averages for the observed $|E_\parallel(E_r > 0)|$ with its surrounding cyan *crown* of the probability surface of occurrence. The red connected diamonds reflect the locus of U binned average values of $\Gamma_\parallel^*(U)$; they are enveloped by the red–white–blue (rwb) *crown* transferred from Figure 14.

Despite the external gradient approximations needed to form $\Gamma_\parallel^*(U)$, five important features of this comparison are notable:

1. The interior of the $|E_\parallel(U)|$ *cyan crown* is in almost all places *inside* the broader $|\Gamma_\parallel^*(U)|$ *rwb crown*; conversely, parts of the $\Gamma_\parallel^*$ crown and red dots are well below the $|E_\parallel(U)|$ *cyan crown*.
2. The 80 binned mean values (blue dots) for $|E_\parallel|$ are *almost entirely within* the $|\Gamma_\parallel^*(U)|$ crown.
3. The wider *crown* of the $|\Gamma_\parallel^*(U)|$ surface and point (1) suggest that not every contributing data point fulfills the assumptions made for the evaluation of $\Gamma_\parallel^*$.
4. However, a large number fraction of the electric field–plasma comparisons that determine the separate crowns shown would appear to be consistent with the expected equality motivated by the leading-order terms of the generalized Ohm's law, Equation (30); this support is better at higher rather than lower speeds.
5. Given the strong dependence of $|\Gamma_\parallel^*|$ on the gradients, the details of overlap of probability *crowns* appear to suggest either (i) that the assumed pressure gradients needed to compute $\Gamma_\parallel^*$ were assumed too small at low speeds, and a little too strong between 500 and 600 km s^{-1}, or (ii) that conclusions from these comparisons may be compromised if *all* the data used are not equally compatible with the gradients $\epsilon_{\chi_r}^*$ assumed prior to making the algebraic comparison.

The general concern about the appropriateness of the *assumed* solar wind gradients for *all* data collected in the solar wind will be explored next as the possible cause of the visual disagreements of Figure 16.

13. Single-radius Determinations of Gradients

Another approach to evaluating the accuracy of $\mathbb{E}_\parallel$ and $E_\parallel$ is a form of *reductio ad absurdum*: assume that the approximate generalized Ohm's law is correct, and use it to infer the required electron 1 au pressure and temperature gradients. Comparisons of these estimates with the reported bulk speed dependence of temperature gradients determined by single power-law fits may produce more secure confirmation or contradiction of the accuracy of the single-point gradients from the Wind 3DP $\mathbb{E}_\parallel$ determinations.

It should be self-evident that the logic of this approach to verification *presumes* that the data sets used are characterizing, or are screened to examine, the same *class of plasmas* and diagnosing them with measurement approaches with comparable spatial and temporal Nyquist conditions. More precisely, different techniques when examined carefully have different limitations, even though they both are said to be characterizing *solar wind plasma properties at 1 au*!

Since Wind 3DP data at the forward Lagrangian point do not determine radial power-law gradients by collecting data while the spacecraft moves in radius, this issue of comparability is of concern. This is not trivially redressed since the literature's method for gradients from fits to radial power laws uses data collected over time and space, while the present paper's technique determines gradients from a single snapshot in time and at a single location in space using a map of the three-dimensional eVDF. Alternately, it is not clear that using any and all data *in* the solar wind with the Wind 3DP approach are equally able to provide information about the long-wavelength biased profiles that would be determined by fitting a single power law to radially separated data. The above considerations could be consolidated into the concept of the aliasing characteristics of the two techniques. As shown below, ensuring this comparability leads to the desired corroboration, but not before.

Still more complicated is the sea of pressure ridge structures in the solar wind; they have a wide variety of scales *and signs* of local power-law exponents. How does the usual power-law gradient fitting process neglect, weight, ignore, or otherwise digest conflicting gradient signs in the data it is asked to fit? How does data binning and a profile's radial extent shape the reported power-law exponent? If the sea of structured pressure signals are organized, they are not well assumed to be Gaussian random noise, as presumed in the usual least-squares procedures. In turn, this implies that the returned fit is not the beneficiary of Gauss's and Legendre's ingenuity that insulates the user from truly random Gaussian noise. What do such fits mean, and what systematic effects do they retain in their numerical values?

13.1. Overview of All Data 1995–1998

Every Wind eVDF algebraically determines a local power-law exponent using Equation (30):

$$\epsilon_{P_{e\parallel},r} \simeq \frac{erE_r}{kT_{e\parallel}} + (1 - \mathcal{A}_e^{-1})\epsilon_{Br}^*. \tag{31}$$

Using all 4 yr of these Wind estimates allows a sweeping view in Figure 17 of the *column-normalized probability of occurrence*, size, and *sign*(!) of pressure exponents of the electron pressure ridges (of the parallel eigenvalue of the pressure tensor) traversed as the sampled wind speed changes. It is important to reemphasize that these column-normalized probabilities are insulated from the unavoidable nonuniformity of Wind sampling with solar wind speed.

In Figure 17 the inferred sizes of the electron parallel pressure exponents span the interval of $-10 \leqslant \epsilon_{P_{e\parallel_r}} \leqslant 10$; the horizontal axis is solar wind speed. The yellow horizontal thin line corresponds to isobaric plasmas, with zero exponent, a regime *inconsistent with a spherically symmetric wind solution*. The black horizontal line at $\epsilon_{P_{e\parallel_r}} = 2$ corresponds to a spherically symmetric pressure profile that has an isothermal temperature profile—a plasma with infinite scale for temperature variation but finite scale for pressure variation. All larger positive values of $\epsilon_{P_{e\parallel}} > 2$ correspond to outward-decreasing, ever-steeper temperature profiles than the flat isothermal temperature profile and ones compatible with near-inverse square density profiles. They have radial pressure scale lengths in au of $L(\text{au}) \simeq 1/\epsilon_{P_{e\parallel}r}$.

Considering the range of USSSW solutions available, the electron temperature profiles near 1 au might have inverse exponents between 0 and 1.33, so that pressure profiles for this type of modeled wind would be found between or near the

interval of exponents in the range $2 \leqslant \epsilon_{P_{e\parallel}r} \leqslant 3.33$. If the wind at 1 au is still accelerating, the upper limit on the pressure exponent might be as high as 4.0.

Considerable information about this 4 yr data set may be gleaned from the colored histogram of probability of occurrence of over a quarter million point determinations of local electron pressure power-law exponents in Figure 17:

1. Over 4 yr there is virtually no inferred column-normalized probability (see Figure 18 as well) for finding these pressure exponents in a very dark band centered on 0 (especially in the most heavily mapped bulk speed states $U < 600$ of this data set). Since Equation (31) algebraically permits such near-zero exponents, the measured $E_\parallel$ is not too small by factors of 2 by this consideration alone. This is physically consistent with the solar wind not ever being isobaric.

2. Taken at face value, there is measurable probability at negative as well as positive exponents $\epsilon_{P_{e\parallel}r}(U)$ in *all* the different bulk speed columns surveyed. Given (1), this result cannot be explained by an incorrect zero-point on the scale that determines $E_\parallel$. This time-averaged probability map of the solar wind generally contains sharp pressure ridges that are locally both *decreasing* and *increasing* with increasing radius. The probabilistic nature of this picture does not require simultaneous positive and negative exponent readings in the same bulk speed column. Minimally it requires that such different sensed gradients in the same flow speeds be recorded at different times.

3. There is an asymmetric ordinate pattern in Figure 17: at all speeds the maximum column-normalized (yellow) probability (across both signs of exponent) decidedly favors. *positive $\epsilon_{P_{e\parallel}} > 1$*. As resolved below in Figure 18, this peak is very sharp with a most probable value just above 2, with over a quarter of a million points in the histogram. This finding is consistent with very frequent, but not exclusive, Wind-SERM detection of pressure scales of the size usually modeled as USSSW, characterized by a generally falling pressure and temperature with increasing radius, corresponding to positive exponents $\epsilon_{P_{e\parallel}r} \simeq 2$ as seen in Figure 17. *Thus, the Wind-SERM $\mathbb{E}_\parallel$* measurements outlined in this paper have identified those eVDF spectra that can infer pressure gradients consistent with being USSSW!

4. In the lower speeds the finite probabilities of the orange–red–green colored regions in Figure 17 extend to exponents with magnitudes beyond the colored histogram's ordinate bound; even at these bounds of this figure the pressure gradient scales are more than 5 times steeper than that implied by the minimum (isothermal) exponent of 2 for spherically symmetric isothermal wind (see Figure 18 for even shorter scales). This enhanced width of probability at shorter scales quickly narrows as the column's wind speed increases, reaching a lower and fairly steady breadth above $450 \, \mathrm{km \, s^{-1}}$. This morphology is consistent with the short scales being preferentially detected in corotational pressure ridges, predominantly possible at 1 au *below* the wind's corotational speed at Earth $U < 450 \, \mathrm{km \, s^{-1}}$.

5. The probability for $|\epsilon_{P_e\parallel r}|$ for these short-scale gradients of both signs appears to cascade toward longer scales (smaller-magnitude exponents) as U increases, consistent

with the expected absence of corotational signatures above $450 \, \mathrm{km \, s^{-1}}$ at 1 au.

6. The dominant scale for negative $\epsilon_{P_{e\parallel}r}$ is 2–3 times shorter than the dominant scale for spherical-wind-like solutions, having exponents of -4 to -10.

13.2. Occurrence of $\epsilon_{P_{e\parallel}} < 0$ and $\epsilon_{P_{e\parallel}} > 0$

Another view of these findings is produced by making separate cumulative histograms of the occurrence of scales first sorted by exponent signs and then binned logarithmically in $|\epsilon_{P_{e\parallel}r}|$. These results are shown in Figure 18 by three superposed histograms: (i) black: all positive exponents; (ii) red: all negative exponents; and (iii) blue: the difference of all positive–negative histograms at the same scaled pressure exponents.

These histograms show how well these determinations: (i) Prefer values in excess of 2–3, where the blue curve for all red-black exponents has its sharpest most probable value; the peak of the negative gradient events definitely occurs at sharper scales than those with exponent 2 (more like 6–7), corresponding to parallel scale lengths 3–3.5 times shorter ($\simeq 0.1$ au) than the pressure gradient scales of more typical spherical wind models, (ii) Have the strongest gradients of both signs (red and black histograms) with occurrence frequencies well matched above $|\epsilon_{P_{e\parallel}}| \simeq 70$, a regime ($\simeq 0.01$ au), well above the range shown in Figure 17; these structures would have scales nearing the correlation length in the interplanetary magnetic field at 1 au (Burlaga 1995), and (iii) Show that the solar wind sampled is a system dominated by scales more sharply centered about $+2$ than the broader original black curve of all positive exponent readings; this suggestion of more frequent USSSW structures within all structures does not exclude the occurrence of not USSSW morphology.

Treating all the quantities across columns of the 2D histogram in Figure 18 produces a cumulative picture of the probability in time of events, seeming to suggest that the cause of sharp short scales (large $|\epsilon_{P_{e\parallel}}|$) is superposed on the more frequent dominant USSSW occurrence of longer scales with smaller $1 < \epsilon_{P_{e\parallel}} < 6$. This is consistent with the solar wind profiles that are generally expected to be present between pressure exponents between 2–4, contributing their dominant scales to the mix in the 96 s data. However, this general expectation is observed intermingled with other structures possessing shorter scales.

Clearly, fitting a *single* exponent power law to Helios data collected over 0.29 au $< r < 1$ au cannot infer these short scales even when traversed. Conversely, the Wind-SERM approach that balances $E_\parallel$ on a 96 s timescale is strongly influenced when it traverses the stronger electric fields associated with the shorter scales in any data series it processes. This reality makes the Wind-SERM electric field measurements as a set open to different interpretations than possible when fitting long time series to a single radial power law—even when both analyses sample the *same* plasma volume. Among these differences will be the range of parallel electric field strengths reported that will be larger for the Wind-SERM methodology than reported by profiles from gradient fit estimates.

14. Reductio ad Absurdum for SERM's $E_\parallel$ Determinations

The hypothesis that short-scale strong $E_\parallel$ detection would interfere with all the $E_\parallel$ data being corroborated by estimates

via $\Gamma_\parallel^*$ or $\mathbb{K}_{P_{e\parallel}}^*/2$ in Figures 14 and 16 suggests that culling all data based on their single-point value estimates of $\epsilon_{P_{e\parallel r}}$ (using the blue high-probability region of Figure 18) would produce a fairer comparison with the (USSSW) biases of published radial power-law fits to the electron temperature in Figure 13. The likelihood for improvement of correspondence is high for two reasons: (i) Power-law fits to radial profiles of $T_e(r, t)$ tend to be made to binned data in r for data that span a significant range ($\simeq 0.5$ au) in $\mathrm{Log} r$ to obtain an acceptably ranked power-law fit. Single power-law modeling is *incapable* of simultaneously inferring scales short compared to the interval of space traversed; furthermore, it is not assured of properly *averaging* out the signals that shorter scale data contribute to the fit. (ii) By editing the higher-cadence Wind data to only retain those single-point gradient observations with pressure exponents within the peak of the blue histogram in Figure 18, there is still a fairly wide range of exponents allowed in the bulk speed windowed histogram, while still having a high level of overdetermination at narrow, well-defined solar wind speed buckets.

The blue histogram in Figure 18 suggests choosing a restricted exponent range like $1.5 < \epsilon_{P_{e\parallel}} < 10$ for admitting 96 s data to obtain wind profile gradient estimates. This filtering approach reduces the size of the 4 yr data set by only accepting points generally more compatible with USSSW concepts than the unedited 4 yr data set. Proceeding with these restricted data determines *overdetermined* average values for $\langle \epsilon_{P_{e\parallel}}(\overline{U}) \rangle$ in narrow Wind speed buckets that cover the observed range of wind speeds.

15. SERM $E_\parallel$ Determines Structureless Solar Wind Gradients

The form of Equation (30) is equivalent to a simple linear equation for the ith 96 s eVDF involving their logarithms:

$$
\begin{aligned}
\ln \mathcal{Y}_i &= M_i + \ln \mathcal{X}_i \\
\mathcal{Y}_i &= erE_r(i) + kT_{e\parallel}(i)(1 - \mathcal{A}_e^{-1}(i)))\epsilon_{Br}^*(i) \\
\mathcal{X}_i &= kT_{e\parallel}(i) \\
M_i &= \ln \epsilon_{P_{e\parallel r}}(i),
\end{aligned} \tag{32}
$$

as algebraically equivalent to

$$
\epsilon_{P_{e\parallel r}}(i) = \frac{\mathcal{Y}_i}{\mathcal{X}_i}. \tag{33}
$$

The form of Equation (32) is appropriate for the Gauss–Legendre fitting/averaging method since E_r and $T_{e\parallel}$ have both been shown to be log normally distributed.

To improve the determination of a suitable best natural log of the positive gradient for the speed bin, $\overline{M}_i(\overline{U}_j)$, within a jth speed interval about $\overline{U}_j$, consider it being overdetermined by the N_j spectra, $i_j = \{1, \dots N_j\}$, whose bulk speeds are in the j'th speed window and admissible from the blue difference histogram of Figure 18. We desire the best least-squares fit solution $\overline{M}_j(\overline{U}_j)$ for

$$
\mathrm{Log} \mathcal{Y}_{i_j} = \overline{M}_j(\overline{U}_j) + \mathrm{Log} \mathcal{X}_{i_j}, \tag{34}
$$

where the indices i of the jth bulk speed buckets are denoted by $i_j = \{1, \dots N_j\}$. The optimal least-squares answer is

$$
\epsilon_{P_{e\parallel r}}(\overline{U})_j = \exp^{\langle M_i \rangle_{i_j}}, \tag{35}
$$

where $\langle \dots \rangle_{i_j}$ denotes the mean value over the N_j i entries i_j in the jth speed interval,

$$
\begin{aligned}
\langle M_i \rangle_{i_j} &= \frac{1}{N_j} \Sigma_{i=1}^{N_j} \ln[\epsilon_{P_{e\parallel r}}(i)] \\
&= \ln [\Pi_{i=1}^{N_j} \epsilon_{P_{e\parallel r}}(i)]^{1/N_j},
\end{aligned} \tag{36}
$$

which is the natural logarithm of the geometric mean of the single-point estimates in the jth speed bucket. This is the same result as averaging the initial formula in Equation (32), assuming that the deviations from the logarithms are Gaussian. The overdeterminancy of these conditions involves $N_j \simeq 2000$ (except at the highest speeds) for a nearly constant bulk speed window, providing unusual clarity of possible bulk speed dependence and strong error reduction. This situation should be contrasted with radial pressure profile fitting that must also *deduce, argue, and defend* that the observed data points acquired at different radial positions are nearly on the same streamline labeled by $U(1$ au$)$ at 1 au, where the observations were not acquired (see Maksimović et al. 2020 for discussion of this style of organization).

The fit uncertainty of $\epsilon_{P_{e\parallel r}}(\overline{U})_j$ is indicated by the red flags in Figure 19. These values were determined by

$$
\delta \epsilon_{P_{e\parallel r}}(\overline{U})_j = \sqrt{\frac{\Sigma_{i,k,m}[\exp^{\langle M_{i_j,k,m} \rangle} - \epsilon_{P_{e\parallel r}}(\overline{U})_j]^2}{100 N_j}}
$$

$$
M_{i_j,k,m} \equiv \ln \left[\frac{\mathcal{Y}_{i_j} + G_m \Delta \mathcal{Y}_{i_j}}{\mathcal{X}_{i_j} + G_k \Delta \mathcal{X}_{i_j}} \right], \tag{37}
$$

where $\Delta \mathcal{Y}_{i_j}$ and $\Delta \mathcal{X}_{i_j}$ are the changes caused by modifying $\overline{E}_{\parallel i_j}$ and $T_{e\parallel i_j}$ by their respective precisions and G_x is the xth of 100 numbers drawn from independent unit variance Gaussian random generators.

To obtain total pressure or total temperature gradients from $\epsilon_{P_{e\parallel r}}$, the relationship (see Equation (A15))

$$
\epsilon_{P_e r} = \epsilon_{P_{e\parallel r}} - \frac{2U\beta}{\mathcal{A}_e(\mathcal{A}_e + 2)} \epsilon_{Ur} \tag{38}
$$

between $\epsilon_{P_{e\parallel r}}$ and $\epsilon_{P_e r}$ is required, where β, defined as

$$
\beta = \frac{d\mathcal{A}_e}{dU} \simeq 8.8 \pm 1.2 \times 10^{-4} \frac{\mathrm{s}}{\mathrm{km}}, \tag{39}
$$

was determined by noting that the observed electron anisotropy varies approximately linearly with the bulk speed (Equation (A17)) and enters the analysis when evaluating

$$
\frac{d\mathcal{A}_e}{dr} \simeq \beta \frac{dU}{dr}. \tag{40}
$$

The results in 76 speed intervals from the generalized Ohm's law yield estimates for $\epsilon_{P_{e\parallel r}}(U)$ (blue diamonds) are shown in Figure 19, together with their related gradient $\epsilon_{P_e r}$ determined from Equation (38).

The black dotted curves that flank a black dashed curve indicate the expected variation of the electron *total* pressure gradient based on empirical T_e power-law fits (illustrated in Figure 13) at different speeds in the solar wind (Maksimović et al. 2020). Although the Figure 13 empirical data determined $\epsilon_{T_e r}$ directly, the curved black dotted region in Figure 19 is

deformed to account for spherically symmetric implied pressure variations according to

$$\ln P_e(\overline{U}) \equiv \ln kT_e(\overline{U}) + \ln n_e(\overline{U})$$
$$\ln P_e(\overline{U}) = \ln kT_e(\overline{U}) + \ln C - \ln U - 2\ln r$$
$$\epsilon_{P_er}(\overline{U}) = \epsilon_{T_er}(\overline{U}) + 2 - \epsilon_{U_r}(\overline{U}). \tag{41}$$

The upper locus from the Wind-SERM approach of this paper for the full electron pressure gradient is fully within the deformed expectation (two black dotted guard band curves) based on Maksimović et al. (2020) empirical collections of power-law fits for ϵ_{T_er}. The top row of Wind-SERM data diamonds represents minor corrections to the lower Wind-SERM trace directly obtained by using $E_\parallel$ and the generalized Ohm's law.

By contrast, Maksimovic's suggested temperature gradients and simple inverse squared corrected pressure gradients were also corrected for the residual acceleration effects that make the density gradient at higher speeds fall off faster than inverse square. The green ramp (with black dashes) in Figure 19 shows this sizable contribution to the indirectly inferred pressure gradients implied by our Helios estimates of this *acceleration* effect at high speeds.

The Wind-SERM electric field determination of the pressure gradients does not differentiate between temperature or density variations as to their cause and at the present level of approximation does not require any modification for the presence or absence of the wind's acceleration; the parallel electric field reflects whatever acceleration has occurred that modifies the steady density profile.

Despite this, the Wind-SERM electric field estimates of $\epsilon_{P_er}(U)$ are clearly compatible with the deformed extensions of the Maksimovic profiles that needed the acceleration modification. The Wind-SERM Maksimović et al. (2020) comparison clearly oscillates about the mean prediction (black dashed curve) implied by the fitted bulk speed dependence (Equation (13)) of the electron power-law data of Maksimović et al. (2020), while indirectly authenticating the model of the acceleration incorporated from unpublished Helios analysis.

Unfolding the acceleration and density gradient from the Wind-SERM electric field determination of the pressure gradient, ϵ_{P_er}, in Figure 19, it is now possible to show in Figure 20 the implied, measured bulk speed dependence of solar wind electron temperature gradient, $\epsilon_{T_er}(U)$. This procedure allows the ultimate comparison with the directly comparable (dashed black curve with dotted black curve guard bands) profile most recently assembled by Maksimović et al. (2020) from radial power-law fits of $T_e(r, \overline{U})$ along surmised streamlines. This favorable contrast is the most incisive test of accuracy of the present determinations of $E_\parallel$ in this paper. By this comparison the Wind-SERM $E_\parallel$ determinations (with $\zeta = 1$) are shown to be at, if not better than, the present state of the art by other means.

The vernier SERM assays in Figure 20 of the bulk speed dependence of ϵ_{T_er} derived from the Wind 3DP data are shown with the red dots, fitted by the best blue curve of the model form indicated. The dispersion of the SERM data points about the blue curve determines the $\pm$ width of the framing red dashed curves.

Several points are clear: (1) the SERM estimates for the bulk speed dependence of ϵ_{T_er} are tightly organized; but most importantly, (2) this pattern winds through the interior of Maksimovic's coarsely determined radial gradients, but is

totally inside its error bounds (black dotted curve), although (3) suggesting a very cohesive and smoother functional dependence on bulk speed. The error flags (4) on the SERM T_e profile $\Delta\epsilon_{T_er}$ are set to be three times the error of the mean. Numerically these errors are those determined for the pressure gradient exponents. These errors represent electron power-law exponent fractional errors nearly the same as the computed spectrum-dependent errors in the input $E_\parallel$. Exceptions occur at extreme high wind speeds, where the electron temperature becomes very cold and where data overdetermination weakens. The SERM estimates (5) have been made with a vernier bulk speed resolution finer than those painstakingly collated by Maksimović et al. (2020).

The bulk-speed-dependent SERM estimates of ϵ_{T_er} reveal a two-zone behavior: with power-law exponents decreasing linearly above $265\,\mathrm{km\,s^{-1}}$, and consistent with being a constant above $530\,\mathrm{km\,s^{-1}}$. For the model hyperbolic form indicated on the figure fitted to the data (blue curve), the high-speed exponent is centered on 0.27 ± 0.04, perhaps accidentally close to the well-known Spitzer-conductivity-dominated two-fluid wind solution with exponent $2/7 = 0.285$. The normalized $\chi^2_\nu = 0.45$ suggests that the model form with its input errors and the data are operationally interchangeable.

Insofar as verifying the accuracy of SERM'S electric field, the comparison in Figure 20 shows that using SERM's stated *precision* as its fit error *accuracy* yields results more coherent and superior to those reported from the corroborating Maksimovic inventory—but nonetheless consistent with its relatively wide tolerances of expectation based on radial power-law fits. Accordingly, the accuracy of the present method for determining $E_\parallel$ and $\mathbb{E}_\parallel$ meets and exceeds the expectations of those parallel radial power-law estimates considered to be the prior zenith of this experimental art.

Together with their error bars, the bulk speed dependence inferred for $\epsilon_{T_er}(\overline{U})$ is totally consistent with all known radial $T_e(r, U)$ profiles for electrons provided that this blue model profile is averaged over the solar wind streamline labeled speeds used in prior studies; generally this information is poorly documented or unknown. These quantitative tests, as well as the global patterns shown in Figure 17 of occurrence and avoidance of different-sized exponents, are strong support that the $E_\parallel$ values reported here are geophysical and have the 10% precision and calibration accuracy suggested.

16. Accuracy Assessment of Wind-SERM $E_\parallel$, $\mathbb{E}_\parallel$

The accuracy of the present approach can be solidified by the following study that was made assuming that the Wind-SERM parallel electric fields were imprecise by a multiplicative factor ζ. This approach allows exploring the relevance of the Fuchs et al. (1986) possibility that $\mathcal{E}_\varpi$ inferred in this paper for each Wind spectra should have been associated with a different theoretical fiducial $\mathbb{E}_\parallel$ (Equation (8) in Fuchs et al. 1986) than the one Dreicer proposed as summarized in Appendix A.3.

Assuming that $\mathcal{E}_\varpi$ and E_D are fixed by the recipe above for the ith eVDF observation, this retrospective reduces to exploring the acceptability in the data corroboration that for *all* eVDF we suppose there exists a factor ζ that is more suitable than the value of $\zeta = 1$, which is Dreicer's recipe, i.e.,

$$E_{i,\parallel}(\zeta) = \frac{3\zeta E_D(i)}{\overline{\mathcal{E}}_\varpi(i)} = \zeta E_\parallel^{\mathrm{Dreicer}}$$
$$0.1 \leqslant \zeta \leqslant 2.1. \tag{42}$$
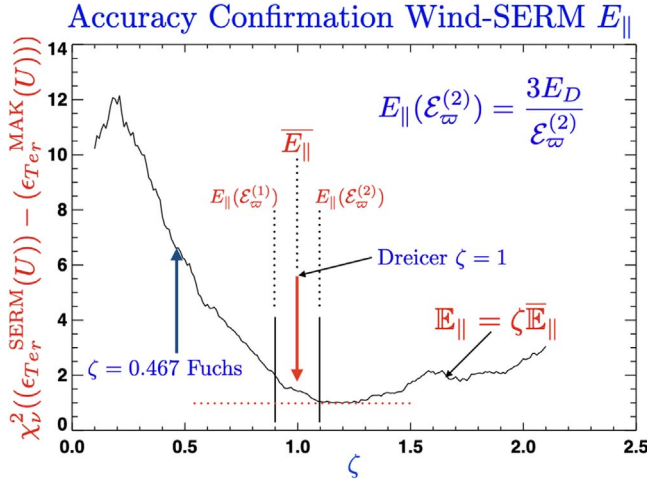
Figure 21. Curve: variation of $\chi^2(\zeta)$ when comparing Wind-SERM $\epsilon_{Te_r}(\zeta)$ with those assembled by Maksimović et al. (2020). Here ζ is the assumed magnification of the computed values for $\overline{\mathbb{E}_\parallel}$ and thus $E_\parallel$ when $\mathcal{E}_\varpi$ remained as operationally implemented above. Note the clear minimum χ_ν^2 within 10% of Dreicer's $\zeta = 1$ and the much higher Fuchs's $\chi_\nu^2(\zeta = 0.467) = 6.5$ that supposed that all Wind-SERM electric fields were 47% smaller than in the histograms in this paper.

The ζ range searched is motivated in Appendix A.3 and envelops both the Fuchs (0.467) and Dreicer (1) hypotheses.

The Wind-SERM temperature gradient exponent calculations were repeated for 200 equi-spaced values of ζ_j to redetermine the 80 bulk speed bucket average values $\langle \epsilon_{Te_r}(\overline{U}, \zeta_j)\rangle$. For each value of ζ_j the bulk speed variation of the implied electron temperature exponents $\epsilon_{Te,r}^{\text{SERM}}(\overline{U}_k, \zeta_j)$ was compared with the bulk speed functional variation $\epsilon_{Te,r}^{\text{Mak}}(\overline{U}_k)$ implied by Equation (26) for temperature gradient exponents assembled by Maksimović et al. (2020). A χ^2 measure of the form

$$\chi_\nu^2(\zeta_j) = \frac{1}{76}\Sigma_{k=0}^{77}\frac{(\epsilon_{Te,r}^{\text{SERM}}(\overline{U}_k, \zeta_j) - \epsilon_{Te,r}^{\text{Mak}}(\overline{U}_k))^2}{\delta\epsilon_{P_{e\parallel}}(\overline{U}_k)^2 + (\Delta/2)^2} \quad (43)$$

was used to explore the sensitivity of this external corroboration to the value of ζ_j assumed. In Equation (43) $\Delta = 0.16$ is the *full* half-width of the ribbon (see Figure 13, which encompassed all errors reported in the Maksimović et al. 2020) data set. The factor $\Delta/2$ in the χ^2 is an attempt to estimate the relevant average of errors given that Δ encompasses *all* 1σ error bars. This is complicated by the inclusion of a range of solar wind speeds in some of the data points summarized in the set.

The variation $\chi_\nu^2(\zeta)$ in Figure 21 shows a very strong preference for ζ near unity and an emphatic rejection of the Fuchs et al. (1986) hypothesis of $\zeta = 0.467$ that might be surmised as possibly relevant to our consideration (see Appendix A.3).

With 75 degrees of freedom there is virtually no expectation for χ^2 to be 6.5 as is required to consider the Fuchs interpretation further for this measurement approach to determining $E_\parallel$.

A possible point of confusion is that although the separatrix speed v_r in Fuchs et al. (1986, Figure 2) is numerically *lower* than Dreicer's v_ϖ (and would ab initio require a larger $\mathbb{E}_\parallel$ to produce), the test being performed by varying ζ is to decide which formula (Dreicer's or Fuchs's) corresponds properly to

the already fixed, operationally determined $\mathcal{E}_\varpi$ and delineated E_D for a given spectrum that do not change as ζ varies in these trials. From this vantage point the requisite size of $E_\parallel(\zeta_j)$ reverts to asking alternate recipes in the same plasma conditions to predict the *same* value for $\mathcal{E}_\varpi$. With this reframing of the algebra,

$$0.81\frac{\sqrt{3}E_D(n_{eo}, T_{eo})}{E^F_\parallel} = \mathcal{E}_\varpi = \frac{3E_D(n_{eo}, T_{eo})}{E^D_\parallel}$$
$$\frac{E^F_\parallel}{E^D_\parallel} = \simeq 0.467 \quad (44)$$

implies that in order to be consistent with $\mathcal{E}_\varpi$ the Fuchs recipe needs a weaker electric field than the Dreicer relation.

Perhaps the strongest experimental statement that can be made is that the operational method that determines $\mathcal{E}_\varpi$ requires the Dreicer relation to relate its size to $\mathbb{E}_\parallel$ to enjoy strong external accuracy corroboration with the Maksimović et al. (2020) inventory as constrained by over a quarter of a million Wind-SERM readings. From this point of view the $\zeta = 1$ minimum in Figure 21 is *expected* as a matter of logical consistency between how $\mathcal{E}_\varpi$ was operationally found and how it should be interpreted.

Nonetheless, the final arbiter of this apparent ambiguity between Fuchs's v_r and Dreicer's v_ϖ is that the logically consistent path is the one that enjoys external accuracy corroboration when comparing with the completely independent methodology used by Maksimović et al. (2020). (This point of view emerged from a helpful discussion with Vadim Roytersheyn and Patrick Killian.)

In this connection it is worthwhile to consider that the estimates of $\overline{E_\parallel}$ in this paper are the average of two slightly different estimates that are statistically $\pm 10\%$ removed from the $\zeta = 1$ values used in most of the figures in this paper. The minimum in Figure 21 at $\zeta = 1.1$ might be interpreted to imply that the higher estimate for $\overline{\mathbb{E}_\parallel}$ within the error bar is slightly more appropriate for electric field magnitudes than the average, and certainly more appropriate than the lower estimate. If true, this corresponds to preferring the average denoted above as $\mathcal{E}^{(2)}$ rather than the impartial average as was done in the analysis section. Since the preference cannot be exhibited without checking for external corroboration done here, this retro-spective insight can be used going forward when archiving the measured electric field strengths and those for $\overline{\mathbb{E}_\parallel}$. The size of this possible systematic error for $E_\parallel$ is proportional to $|1 - \zeta_{\min}|$; this accuracy error is thus within the already tabulated reproducibility percentage error for $\overline{\mathbb{E}_\parallel}$ precision shown in Figure 12. For archival purposes this study suggests vernier modifications of the best Wind-SERM electric field estimates according to

$$\overline{E_\parallel} \rightarrow \frac{3}{\mathcal{E}^{(2)}} \simeq 1.1\ \overline{E_\parallel}(\zeta = 1)$$
$$\overline{\mathbb{E}_\parallel} \rightarrow E_D\ \overline{E_\parallel} \simeq 1.1\ \overline{\mathbb{E}_\parallel}(\tau = 1). \quad (45)$$

The variation of all known solar wind radial $\epsilon_{Te_r}(U)$ profiles for electrons is compatible with the vernier profiles shown in Figure 21. The χ^2 test of Figure 21 and other quantitative tests, as well as the global patterns of occurrence and avoidance of different-sized exponents shown in Figure 17, are all strong support that the $E_\parallel$ values reported here are physical with the 10% precision and accuracy claimed.

17. Suprathermal Hardness and $\mathbb{E}_\parallel$

Power laws in the eVDF are routinely presumed to be present for remote plasma radio and X-ray emission scenarios. Phenomena involving power-law forms usually assume that these nonthermal features are by-products of $E_\parallel$ accelerations that deform the Maxwellian shape. Dreicer realized more than 60 yr ago that *any* $E_\parallel$ promotes some electrons out of the thermal population, forming local runaways that can be the origins of nonthermal velocity distribution functions. As the size of $\mathbb{E}_\parallel$ increases, the fraction of electrons promoted by this process is expected to grow rapidly (Dreicer 1959, 1960; Fuchs et al. 1986; Scudder 1996). The general argument that quasi-neutrality requires $\mathbb{E}_\parallel \simeq \mathcal{O}(1)$ in astrophysical plasmas and the broad arguments in Scudder (2019b) suggest looking for a correlation in the Wind data between *local* suprathermal spectral hardness and the *collocated estimate* of $\mathbb{E}_\parallel$ available in this paper.

The Wind 3DP solar wind eVDF at suprathermal energies is routinely fit by a fixed power law that allows for anisotropic most probable speeds (Salem et al. 2021). The κ parameter is determined as a least-squares fit parameter at the high energies of the halo subcomponent considering *all* pitch angles. In fact, the recently proposed SERM (Scudder 2019b) suggested that the cause for the nonthermal leptokurtic eVDF at 1 au is a steady variant of the physics used to explain laboratory runaway phenomena (Dreicer 1959; Fuchs et al. 1986); it naturally predicts the hardening of the suprathermal fraction with increasing $|\overline{\mathbb{E}_\parallel}|$.

A spectral hardness index, $\mathcal{H}$, of the form

$$\mathcal{H} \propto (\kappa_h^{-1} - 0.1) \qquad (46)$$

has been used. Operationally with typical eVDF resolution it is very difficult to distinguish eVDFs with best fit κ values bigger than 10 from being a Maxwellian. This sets the constant -0.1 in the formula to compute $\mathcal{H}$. The form computes an *increasing* hardness $\mathcal{H}$ for *decreasing* $\kappa < 10$. In the 4 yr data set fit κ ranges between $2.5 < \kappa < 10$, with typical values in the 5–6 range. Since the Wind 3DP data processing predated the techniques of this paper being able to measure $\mathbb{E}_\parallel$, there is no experimental interdependence of the power-law exponent or size of $\mathbb{E}_\parallel$.

The 2D spectrogram summary of $\mathcal{H}(\mathbb{E}_\parallel)$ versus $\mathbb{E}_\parallel$ for 279,807 spectra is shown in Figure 22; by its column normalization it removes the oversampling of typical conditions and provides the probability for detection as a function of ordinate and abscissa pair. For easy reference the locations of different-sized κ values are indicated by cyan numerals along horizontal dashed black lines. The highest hardness values recorded begin to challenge the domain where a formal nonrelativistic kappa function has divergent moments and thus needs to be generalized for relativistic effects.

The blue diamond tagged trend of the column averages of $\mathcal{H}$ in the spectrogram does show that the Wind 3DP recorded electron suprathermal spectral hardness does increase with increasing $\mathbb{E}_\parallel$, as expected. When kappa approaches 3.5 in the Wind data, the dimensionless parallel electric field nears its largest observed values, $\mathbb{E}_\parallel \rightarrow 2.5$: the larger readings of $\mathbb{E}_\parallel$ do accompany the harder spectral mean values of $\mathcal{H}(\mathbb{E}_\parallel)$, providing further evidence that the wind $\mathbb{E}_\parallel$ data are physically corroborated in an expected way.
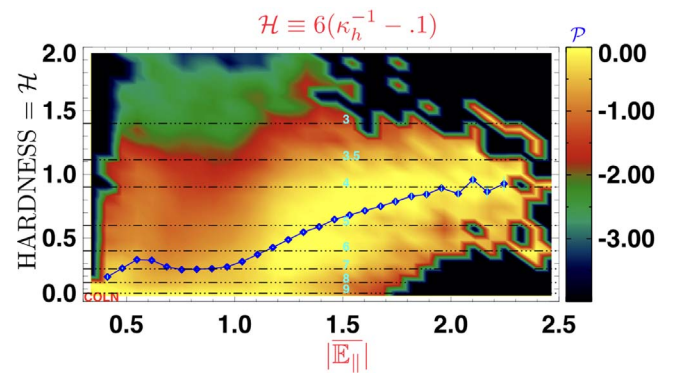
Figure 22. Two-dimensional histogram of the common logarithm of the column-normalized probability of detection of the solar wind halo suprathermal hardness, $\mathcal{H}$ (*y*-axis), as a function of colocated Wind-SERM measurements of $\mathbb{E}_\parallel$. Blue traces demonstrate the expected increase of measured Wind 3DP $\mathcal{H}$ with colocated Wind-SERM values of $\mathbb{E}_\parallel$ (horizontal axis). This behavior is consonant with Dreicer's view of suprathermal tail formation being a sensitive and increasingly important factor with increasing $\mathbb{E}_\parallel = \mathcal{O}(1)$, a behavior internal to the SERM model for solar wind electrons (Scudder 2019b). Dotted black horizontal lines are labeled by fixed corresponding value of κ_h (in cyan) found when fitting the halo population of the Wind 3DP eVDF.

## 18. Strahl Knows about $\mathbb{E}_\parallel$

Evidence is now presented to show that the observed strahl feature of the solar wind eVDF is *cognizant* of, if not strongly organized by, the size of $\mathbb{E}_\parallel$. Located in just the right energy range, the strahl plays an important role in the determination of the heat flux that is thought to be so important in sustaining the solar wind expansion. By its nature $\mathbb{E}_\parallel$ indexes the relative importance of coulomb drag versus $E_\parallel$ accelerations in the plasma; until very recent modeling the strahl subcomponent has been viewed as a feature of the collisionless exospheric model using the method of characteristics, essentially treating the plasma as if $\mathbb{E}_\parallel \gg \gg 1$, if not infinite.

Observationally the observed strahl features on the eVDF are found along the magnetically aligned heat flux direction, but 180° away from those opposed parallel speeds of the eVDF where the size of $\mathbb{E}_\parallel$ has been gleaned (see Figures 3, 2, 23).

The strahl *data inventories* in the Wind 3DP analysis predate and have no knowledge of the subsequent determinations of $\mathbb{E}_\parallel$ presented in this paper. Despite this independence, strong quantitative organization of strahl properties and velocity space extent at the 90% level across 4 yr of data are demonstrated. This is shown by comparing the strahl's phase-space location with those of the interior of the runaway separatrix $\mathbb{S}_F(\nu)$ determined by the $\mathbb{E}_\parallel$ measured for the *same* eVDF. Unlike the canonical model of the strahl as a collisionless vestige of coronal boundary conditions, these observations suggest that *even* at 1 au there is strong coulomb collisional modification, if not control, of the strahl. It is altogether possible that the observed strahl subcomponent is just the odd Legendre skewness residual of plasmas with large $\mathcal{O}(1)$ Knudsen numbers.

### 18.1. Separatrix Boundary $\mathbb{S}(\mathbb{E}_\parallel)$

The coulomb boundaries determined by $\mathbb{E}_\parallel$ from Figure 2 are extracted here to compare with observed strahl properties reported from Wind 3DP observations; these are synthesized from the strahl's first four moments of density, n_s, drift in the ion frame, U_{ds}, and gyrotropic pressures $P_{s\parallel}$, $P_{e\perp}$. The black ellipse is a bi-Maxwellian *shaped* phase-space density that
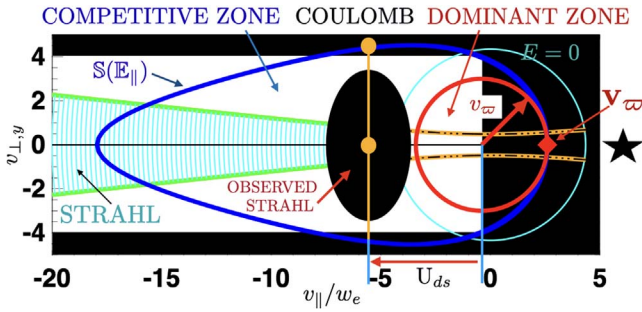
Figure 23. Detected Wind 3DP strahl eVDF (black ellipse centered on its drift speed U_{ds} in the ion frame and extending by one parallel and perpendicular strahl thermal speed from its peak at the bulk velocity) is found almost entirely with the *blue* separatrix $\mathbb{S}$, but outside the coulomb dominant sphere *red circle* at low energies where coulomb collisions compete favorably with $E_\parallel$. Within this red circle dynamics is critically damped by coulomb drag. A drifting nearly isotropic Maxwellian is expected within this red circle. Inside the blue $\mathbb{S}$, but outside the red circle, coulomb drag is still competitive with other forces. Outside $\mathbb{S}$ electric field has driven particles locally into runaway, where they are underdamped by the weakened residual coulomb collisions. The black ellipse denotes the observed location of strahl with its measured drift speed with respect to the ions of U_{ds}, density, and anisotropic effective pressure with $P_{s\parallel} < P_{s\perp}$. As shown, the typical Wind strahl distribution is broader in $T_\perp$ than $T_\parallel$ and the perpendicular strahl thermal speed is invariably smaller than the half-width of $\mathbb{S}$ determined by the distance between the two yellow filled circles, which is the half-width of $\mathbb{S}$ at $v_\parallel = U_{ds}$. This implies that essentially all strahl density is found by Wind 3DP to be within the coulomb separatrix $\mathbb{S}$ determined by the recently measured $E_\parallel$.

numerically has the same moments of the strahl features identified on Wind; the perimeter of the ellipse is at one *e*-folding below the peak that occurs at $v_\parallel - U_{sw} = U_{ds}$, $v_\perp = 0$. Indicated in this cartoon are two yellow dots that bound the perpendicular half-width of the tear draped separatrix curve $\mathbb{S}_F$ at the parallel drift velocity equal to the strahl's drift displacement, U_{ds}, along the magnetic field. The relative size of the strahl black ellipse, the bounds of the red sphere of radius v_ϖ, and $\mathbb{S}_F$ correctly portray the following quantitative statistical properties across the 4 yr surveyed: (i) the observed strahl is found almost always *outside* the red sphere of radius $v_\varpi(E_\parallel)$, and almost always well *inside* the (blue) separatrix $\mathbb{S}_F(E_\parallel)$. These boundaries are determined anew for each eVDF in the data set. As a result, nearly all the identified *strahl signatures*, including the determinants of its density, satisfy these two conditions and are shown to be enclosed *within* the coulomb competitive, or transport domain that is interior to $\mathbb{S}_F$. Such a finding contrasts strongly with the often used model for the strahl as a collisionless feature with anecdotal collisional effects superposed.

If the strahl were aptly described as collisionless, it should be observed where coulomb collisions are unimportant. Yet the strahl is detected within the *closed* runaway separatrix $\mathbb{S}_F$, a locale where significant coulomb scattering and drag are involved in keeping electrons localized *inside* $\mathbb{S}_F$. The antithesis of runaway is a generalized transport regime (inside the separatrix) where the possibility of $E_\parallel$ promotion into runaway has been strongly shunted by coulomb collisions. Despite this ongoing collisional competition, it is not so overpowering as Dreicer had argued would characterize electron populations with speeds $v < v_\varpi(E_\parallel)$ (inside the red sphere) where collisions are so vigorous they *determine* the local form of the eVDF to be a local convected Maxwellian.
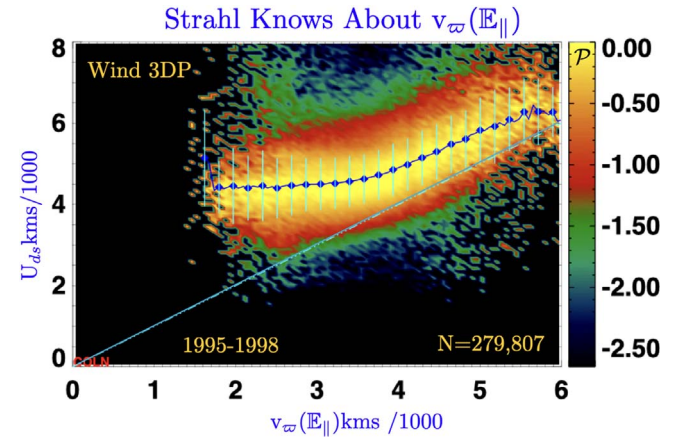
Figure 24. Overview of the size of strahl drift speed and the radius of the (red) spherical boundary in Figure 23 within which coulomb collisions are dominant. The inclined cyan line shows that the strahl bulk speed is invariable outside the sphere of coulomb dominance, whose radius $v_\varpi(E_\parallel)$ is numerically determined by the inventory of this paper that quantifies $E_\parallel$.

18.2. Strahl Is Located outside $v_\varpi(E_\parallel)$

Two quantities that are properties of the eVDF from opposite projections along $\hat{b}$ are the strahl's bulk speed U_{ds} and the location where the minimum runaway speed $v_\varpi(E_\parallel)$ is identified and thus $E_\parallel$ is empirically constrained. These two observables *in the same eVDF* are independent in the experimental sense. However, 4 yr of observations show that these observables are correlated as shown in Figure 24, with $U_{ds} > v_\varpi$, but with the inequality narrowing as v_ϖ gets larger (when $E_\parallel$ becomes smaller in the data set). The 2D histogram illustrates the frequency of occurrence of the time-synchronous observables: $v_\varpi(E_\parallel, t)$, $U_{ds}(t)$. The probability of occurrence is column normalized in narrow bins of v_ϖ, with bright yellow colors denoting the vicinity of maximum probability within the column and thus across columns; darker colors code logarithmically lower columnar probabilities. This 4 yr synthesis shows the common occurrence of the strahl bulk speed leading the boundary of the overdamped coulomb regime indicated by the red sphere in Figure 23. The separation of U_d and v_ϖ is clarified in Figure 25, where local variables are used to construct the parallel separation $S_\parallel$ given by

$$S_\parallel \equiv \frac{U_{ds} - v_\varpi}{w_{s\parallel}} \simeq \mathcal{O}(1), \qquad (47)$$

showing it to be of order the simultaneously inventoried parallel thermal spread of the strahl, $w_{s\parallel}$.

Because it is identified by subtraction (see Salem et al. 2021), the peak of an identifiable strahl phase-space population is displaced from the origin (see Figure 1), standing in phase space with a bulk speed comparable to its *observable* thermal half-width plus v_ϖ along the magnetic field. Thus, its operational form is centered on its inferred moment bulk speed with an extent of the order the thermal spread determined from the moments over the culled phased density. From this perspective the Wind 3DP strahl description flags features in the eVDF with widths in parallel and perpendicular directions to $\hat{b}$ of essentially the moment inferred velocity space dispersions about the moment drift speed, U_{ds}. From this viewpoint the low-speed side of the strahl phase space is statistically located in the ion rest frame of order one parallel
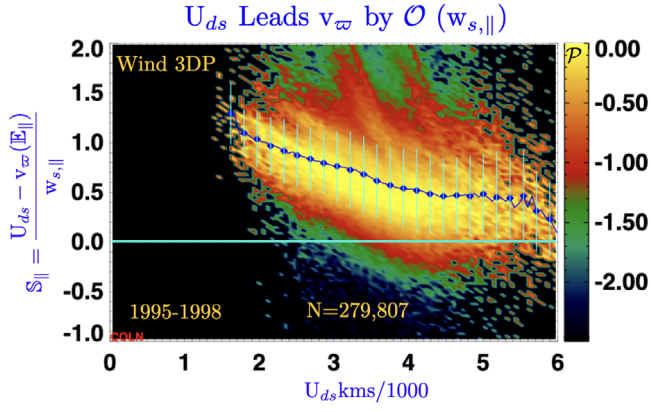
Figure 25. Wind strahl measured to have bulk speed U_{ds} displaced from the proton rest frame by parallel speeds at $v_\parallel \gtrsim v_\varpi + \mathcal{O}(w_{s,\parallel})$. This localizes the strahl as outside of the sphere of radius $v = v_\varpi$, where coulomb collisions are dominant and produce nearly isotropic convecting Maxwellians. The cyan horizontal line corresponds to the strahl bulk velocity being at the outer radius of the collisionally dominant sphere.
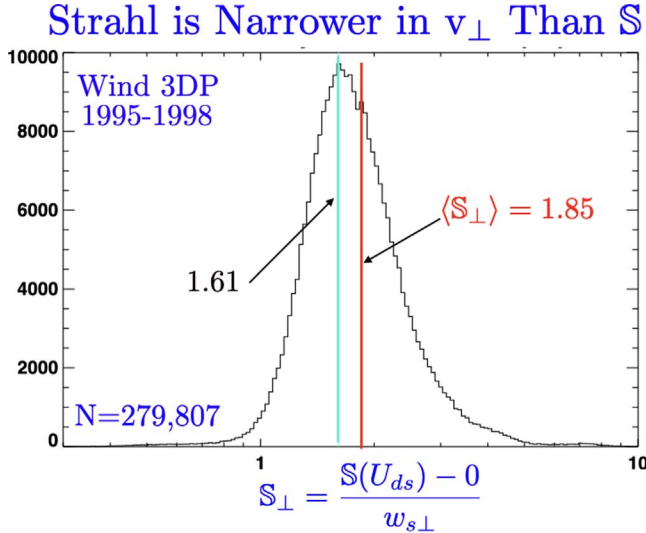

Figure 26. Statistical assay of perpendicular distance $\mathbb{S}_\perp$ of the strahl peak from runaway separatrix in units of the strahl's moment perpendicular thermal speed. Modal values are 1, and the average is 1.85, indicating that routinely the separatrix is more than one and one-half strahl perpendicular thermal speeds displaced from the peak of its phase-space density at $v_\parallel = U_{ds}$, $v_\perp = 0$.

strahl thermal speed below its bulk velocity, satisfying $U_{ds} - w_\parallel \simeq \mathcal{O}(v_\varpi)$. This in turn leads to the coordinated behavior recorded in Figure 25.

18.3. Strahl Is Located inside $\mathbb{S}_F(\mathbb{E}_\parallel, U_{ds})$

In a similar vein, it is of interest to ascertain where the Wind 3DP strahl phase density is located in relation to the half-width of the runaway separatrix, $\mathbb{S}_F$, measured perpendicular to $\hat{\boldsymbol{b}}$ at $v_\parallel - U_{i,\parallel} = U_{ds}$ out to $\mathbb{S}_F$; this distance may be visualized as the separation between the two yellow dots shown in Figure 23.

This distance has been computed for every spectrum (using its own values of $\mathbb{E}_\parallel$ and its *own* separatrix curve $\mathbb{S}(\mathbb{E}_\parallel)$) and contrasted with the observed Wind 3DP *strahl's perpendicular* thermal width, $w_{s\perp}$. For this purpose we define the perpendicular
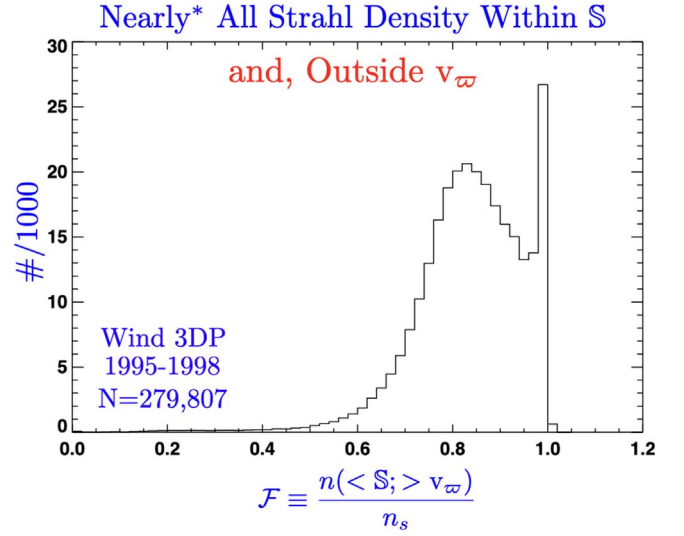
Figure 27. Probability distributions over 4 yr of the fraction of strahl's moment density *inside* the separatrix and outside the sphere where collisions are dominant. Modal value is 100%, and the fraction above 80% is nearly 95% of more than a quarter million spectra.

dimensionless distance

$$S_\perp \equiv \frac{\mathbb{S}(\mathbb{E}_\parallel, U_{ds}) - 0}{w_{s\perp}}, \qquad (48)$$

where the numerator is the distance between the two yellow dots in Figure 23. A histogram of $S_\perp$ covering this 4 yr Wind data set is shown in Figure 26. Although not Gaussian, the mean (1.85) and mode (1.61) plus the shape provide convincing statistical evidence that the observed Wind strahl signatures are narrower than the newly determined operational half-width of the runaway separatrix curve, $\mathbb{S}_P(U_{ds})$, that passes through the strahl bulk speed implied by the separation of the yellow dots shown in this figure.

18.4. Strahl Density Fraction outside v_ϖ but inside $\mathbb{S}$

Figures 23–26 suggest that *nearly all* of the strahl's density reported in the Wind 3DP moments is localized *within* the blue runaway separatrix $\mathbb{S}(\mathbb{E}_\parallel)$, but outside the red sphere of radius v_ϖ bound of Dreicer's collisionally dominant zones; these boundaries are both theoretically determined for the first time by the newly available value of $\mathbb{E}_\parallel$ of this paper.

A bi-Maxwellian phase-space density with moments equal to the numerically reported moments of the strahl *subcomponent* was used to numerically determine the partial density $n_{s,\text{part}}$ of strahl electrons *outside* the red circle, but *inside* the blue separatrix curve $\mathbb{S}_F$ in Figure 23. This integral was determined for each of the more the quarter million spectra using their own newly available values of $v_\varpi(\mathbb{E}_\parallel)$ and their separately delineated runaway boundary curve, $\mathbb{S}(\mathbb{E}_\parallel)$. From these boundaries the strahl density fraction inside $\mathbb{S}_F$ but outside $v = v_\varpi$ was determined and is summarized in histogram form in Figure 27 after normalizing by the reported moment density, n_s, of the Wind 3DP data inventory (Salem et al. 2021). This statistical assay of the density fraction inventoried in this manner quantifies our conjecture that the distributed Wind strahl subcomponents observed are nearly always found within $\mathbb{S}_F$ with speeds outside ν_ϖ in the ion rest frame, as is implied by the black ellipse in Figure 27.

19. Discussion and Conclusions

1. For the first time a method to measure ambipolar $E_{\parallel} \simeq 0.1$ nV m^{-1} using the three-dimensional *shape* of the eVDF at a single spatial location has been developed. The measurement technique exploits Dreicer's ([1959](#), [1960](#)) description of the signatures of $E_{\parallel}$ in the eVDF that are embedded in the recent SERM model for solar wind electrons (Scudder [2019b](#)). The technique is proofed, calibrated, and corroborated with a survey of 4 yr of Wind 3DP electron data and intracomparison with spatial gradient observables not ordinarily available to an essentially radially fixed spacecraft like the GGS Wind vehicle.

2. The direct observable is Dreicer's dimensionless parallel electric field $\mathbb{E}_{\parallel}$ and does not suffer from the usual issues of trigonometry when inferring the very small magnetic-field-aligned component of much larger $\boldsymbol{E}$.

3. The *precision/reproducibility* of the $\mathbb{E}_{\parallel}$ determinations is computed across 4 yr of data to be 10% and the *accuracy* demonstrated by external corroboration to be at essentially the same level.

4. The technique has been used to segregate Wind time series into intervals that objectively have scales long enough to be those of the USSSW of solar wind modeling. When Wind-SERM temperature gradients across 4 yr of data collection are determined from USSSW intervals, they are *well within* and more precise than the error bars of the most recent published electron temperature gradients as a function of bulk speed. While the USSSW intervals found with this new technique predominate in the 4 yr data set, the proliferation of intervals with being USSSW intervals complicates inventories of the solar wind properties. In a generalized way the existence of these inconsistent intervals is a form of *aliasing* not widely considered before when comparing solar wind data products and simplified theoretical models.

5. The observations in intervals inconsistent with being USSSW contain much shorter scale structures with steeper radial gradients of *both* signs and stronger $E_{\parallel}$. Morphologically these intervals principally occur for solar wind speeds ($U < 450$) where corotational pressure effects appear to disrupt the smooth picture of USSSW usually modeled or presumed to be appropriate for continuous time series in the solar wind. Scales approaching the previously known 1 au estimates of the correlation length in the magnetic field have been determined in these regimes using the Wind 3DP data.

6. Over the 4 yr Wind data interval the mode of Wind-SERM $E_{\parallel}$ and $\mathbb{E}_{\parallel}$ had average and modal values of 0.12 nV m^{-1} and $\simeq 0.8$, respectively. Peak amplitude samples and the mode of both quantities of unfiltered surveys were impacted by no USSSW intervals in the data. The observed size of $E_{\parallel}$ is generally a decreasing function of solar wind speed, while $\mathbb{E}_{\parallel}$ is a slowly increasing function of solar wind speed. When restricted to locales where only USSSW gradients are inventoried, the distribution of $\mathbb{E}_{\parallel}$ is still $\mathcal{O}(1)$ and strong in Dreicer's sense, supporting the premises and implications of the recently proposed SERM (Scudder [2019b](#)).

7. When focusing on USSSW regions, the size of $E_{\parallel}$, the generalized Ohm's law, and the remaining local Wind moment quantities have been used to determine the bulk speed variation of the electron temperature gradient (i) with vernier resolution exceeding all known reports, (ii) with accuracy higher than that reported by the most recent collection of radial profile fits, (iii) that are completely consistent with these coarser profiles, and (iv) that are tightly coherent in a two-zone model showing that the electron temperature gradients depend on bulk speed described by one branch of a hyperbola (see Figure [20](#)). The magnitudes of gradients decrease nearly linearly between 260 and 530 km s^{-1} and then level off at a constant value with a radial exponent 0.27 at higher 1 au speed. These comparisons dramatically illustrate the accuracy of the parallel electric field determinations of the Wind-SERM approach; they determine from single-point measurements the value of the power-law exponent gradient only possible after multiple orbital radial traverses by Helios and Parker Solar Probe. This approach is only possible when the Wind data are prescreened against the steep gradients and strong $E_{\parallel}$ found in non-USSSW intervals. These corroborations establish the 10% *accuracy* of the determinations of the Wind-SERM approach.

8. The short-scale structures encountered even show local variations with radius of the opposite sign to that anticipated in the widely considered spherically symmetric wind profiles. A simple model suggests how these effects are readily expected for the present Wind-SERM methodology that *measures* the local gradients of pressure; however, they are produced. Candidates for these shorter-scale compressive structures are those produced by the inhomogeneities of corotating stream interactions being swept past the spacecraft.

9. The theoretically expected enhanced hardness of suprathermals with increasing $\mathbb{E}_{\parallel}$ implicit in the runaway phenomena Dreicer described has been demonstrated using colocated data across the entire 4 yr period. The inverse of the κ power-law strength parameter is converted to measure the hardness of the spectrum and shown to be positively correlated with increased size of $\mathbb{E}_{\parallel}$ (see Figure [22](#)). Spectra with the lowest κ values and highest hardness do indeed systematically accompany the stronger values of $\mathbb{E}_{\parallel} \simeq 3$.

10. These large-scale quantitative tests involving coulomb separatrices clarify that the strahl at 1 au is found in a locale where collisions still compete successfully with, but do not overpower, other forces as they do inside red Dreicer's sphere (see Figure [23](#)) at low energies. The Wind 3DP strahl is observed in velocity space, where coulomb collisions *compete* with the tendency to follow strictly the characteristics of the exospheric model. Most certainly the observed strahl at 1 au is found where finite Knudsen number transport determines its properties rather than the scatter-free picture of the collisionless exospheric explanation. Weak promotion of the strahl into the halo via runaway might occur with as much as 10%–20% of the strahl's density that is approaching the $\mathbb{S}_F$ boundary with $v_{\parallel} \simeq U_{ds}$. The strahl is collisionally exchanging momentum and energy principally with other electrons in the interior of the blue $\mathbb{S}_F$ separatrix; in this way the identified strahl subcomponent is mixing with, or even a part of, the nominal halo subpopulation along the

heat flux axis within $\mathbb{S}_F$. The very small number of strahl electrons promotable by runaway across the $\mathbb{S}_F$ boundary will be a source for the omnipresent halo electrons routinely seen. It is possible that the role of coulomb collisions neglected in almost all strahl-driven instability calculations explains the absence of the predicted whistler turbulence recently reported on Parker Solar Probe (Cattell et al. 2022).

11. These organizational questions underscore the less than clear observational distinction of the various subcomponents of the observed eVDF. In fact, the strahl is identified in Wind 3DP data processing as a locale where the simplicity of the fitted core and halo subcomponents do not resemble the observed eVDF. Since the fitted core and halo models are rather simple even functions of $v_\parallel$ and $v_\perp$ in their own drifting frames, virtually any *odd-order Legendre* needed pitch-angle dependence to support the heat flux and thermal force effect in the observations requires either (i) more complicated core and halo model forms or (ii) as with Wind 3DP data processing, the creation of another category termed *strahl* where all unfit anomalies are aggregated. Thus, the mere existence of a catalog of strahl signatures is a concession that the core and/or halo model forms are incomplete descriptions of the finite Knudsen number deformations of the eVDF in the heat-carrying domain.

    The organizational picture (permitted here by measuring $\mathbb{E}_\parallel$) of the strahl phase space being within $\mathbb{S}_F$ and outside the collisionally dominant ($v > v_\varpi$) region provides an impetus for the idea that the strahl's distinctiveness is more reflective of core and halo fit model simplicities than an endorsement of the strahl as a certain collisionless remnant of the inner boundary condition of the solar wind expansion. On the other hand, the collisionless boundaries can still leave their imprint; the present work raises the question whether the imprint remains sufficiently clear as to be invertible for remote information gathering.

12. The statistical properties of the velocity space location of the Wind (3DP) strahl in relation to the red sphere $v = v_\varpi$ shown in Figures 24 and 25 by themselves are not quantitatively invertible to what eVDF feature(s) are identifiable as being at $v = v_\varpi$. It should be noted that the bulk speed of the strahl is not the peak of the eVDF in the strahl energy range. The bulk speed of the Wind 3DP strahl is only the center of the excess eVDF above and beyond that predicted by the core and halo model, which must first be subtracted to reckon the size of U_{ds}. That such a strahl bulk speed exceeds a defensible estimate of v_ϖ is of course informative, but is it actionable? Even Figure 25 shows that the rms $w_{s\parallel}$ is *only approximately* the distance between the speed U_{ds} and the v_ϖ red circle in Figure 23. Because $w_{s\parallel}$ is determined also as a moment quantity, the connection of this number to the geometrical deformation of the eVDF is by no means straightforward, since the underlying shape that determines these moments is not invertible from this pattern of moments. This, too, makes it virtually impossible to transfer quantitatively the impressions of the Wind 3DP trends seen in Figures 24 and 25 to a general algorithm on another spacecraft that seeks to identify a feature on an otherwise general eVDF where the strahl's lowest energy extremity is found.

Complications of this type make it difficult to translate the Wind 3DP findings about the localization of the strahl into algorithms to identify v_ϖ via phase-space signatures at strahl pitch angles that has been attempted by Berčič et al. (2021). By contrast, the present paper's SERM-Wind technique appropriate for the opposite magnetic field direction from the heat flow has been shown to be corroborated by other observations that are related to the size of $E_\parallel$. It would appear that using the Wind-SERM technique at these opposite pitch angles on PSP spectra from where the strahl boundary has been identified could usefully comment on the systematic quality, or lack thereof, of such procedures employed by Berčič et al. (2021).

13. The three corroborations in the present paper involving electron gradients, hardness, and organization of strahl kinematics produce strong ancillary testimony about the accuracy and reliability of the new Wind-SERM technique developed in this paper to quantify the size of the $0.1 \, \mathrm{nV \, m^{-1}}$ ambipolar $E_\parallel$ and the size of its very strong dimensionless variant, $\mathbb{E}_\parallel$. The strahl finding also shows that there is a middle ground between Maxwellians everywhere based on collisional dominance and a remainder where collisionless exospheric theory reigns. This intermediate regime copes with strong forces and collisional drags and energy losses that are neither perturbative nor dominant, but nonetheless competitive in the determination of kinetic equilibrium throughout the strahl energies where the heat flux moment is determined.

14. The energy transport in hydrogenic plasmas is intimately determined by describing almost all the electrons well—not only where all the density is located, but also where all the energy is carried—while simultaneously not permitting parallel current, and still remaining a quasi-neutral shield for the ions. With the presently documented ability to measure $E_\parallel$ and $\mathbb{E}_\parallel$ it is possible to evaluate more fully the premises and predictions of SERM (Scudder 2019b): does the electron transport modified eVDF reflect the presence and finite (nonperturbative) size of $E_\parallel$ whose presence and approximate size are not negotiable, but set by the omnipresence of mass dependence forces that are unavoidable on the astrophysical stage? In sequels this inquiry continues.

Appendix

A.1. Full Dreicer Formulae

Dreicer's variables and their abbreviations as used in the text are fully defined here in terms of customary CGS variables. The *equality* of E_D used in this paper and E_c by Dreicer (1959, 1960) are also stipulated. The $\ln\Lambda$ expression alone is written in terms of temperature $\mathbb{T}_e$ in eV units rather that in CGS units that is indicated elsewhere by T_e:

$$w_e \equiv \sqrt{2kT_e/m_e}$$
$$\ln\Lambda_c^{e-i} = \frac{47}{2} + \ln[\mathbb{T}_e^{\frac{5}{4}} n_e^{-\frac{1}{2}}]$$
$$\qquad\qquad - \frac{1}{2}\sqrt{(-1 + \ln\mathbb{T}_e^{\frac{1}{2}})^2 + 10^{-5}}$$
$$\equiv \ln\Lambda$$
$$\lambda_{\mathrm{mfp}}(w_e, i) \equiv \frac{(kT_e)^2}{\pi n_e e^4 \ln\Lambda} \equiv \lambda_{\mathrm{mfp}}$$
$$\nu_{ei}(w_e) \equiv w_e/\lambda_{\mathrm{mfp}} \equiv \nu_{ei}$$
$$E_c \equiv E_D$$
$$|e|E_D \equiv m_e w_e \nu_{ei} = \frac{2kT_e}{\lambda_{\mathrm{mfp}}}$$
$$= \frac{2\pi n_e e^4 \ln\Lambda}{kT_e} \propto \frac{n_e}{T_e}. \tag{A1}$$

The form above for $\ln\Lambda_c^{e-i} = \ln\Lambda$ provides a continuous formula across the quantum mechanical regime, $\mathbb{T}_e \simeq 10$ eV, and represents an essentially equivalent form to two separate equations (Fitzpatrick 2015, p. 64, Equation (3.124); also Spitzer 1967, p. 126) needed for Wind plasma.

A.2. Reduction of the Divergence of $\mathbb{P}_e$

The divergence of the gyrotropic electron pressure tensor $\mathbb{P}_e \equiv P_{e\parallel}\hat{\boldsymbol{b}}\hat{\boldsymbol{b}} + P_{e\perp}(\mathbb{I} - \hat{\boldsymbol{b}}\hat{\boldsymbol{b}})$ is given by

$$\nabla \cdot \mathbb{P}_e = \nabla P_{e\perp} + G\frac{(\boldsymbol{B}\cdot\nabla)\boldsymbol{B}}{B^2} - \frac{2G}{B^3}(\boldsymbol{B}\cdot\nabla B)\boldsymbol{B}$$
$$+ \left[\frac{\boldsymbol{B}}{B^2}\cdot\nabla(G)\right]\boldsymbol{B}, \tag{A2}$$

where $G \equiv P_{e\parallel} - P_{e\perp}$. Its magnetic projection is

$$\hat{\boldsymbol{b}}\cdot\nabla\cdot\mathbb{P}_e = \frac{dP_{e\parallel}}{ds} - G\frac{d\ln B}{ds}; \tag{A3}$$

in terms of anisotropy, $\mathcal{A}_e \equiv P_{e\parallel}/P_{e\perp}$, it reduces to

$$\hat{\boldsymbol{b}}\cdot\nabla\cdot\mathbb{P}_e = \frac{dP_{e\parallel}}{ds} + \frac{P_{e\parallel}(1-\mathcal{A}_e)}{\mathcal{A}_e}\frac{d\ln B}{ds}. \tag{A4}$$

A.3. Dreicer and Fuchs Descriptions of Runaway

Dreicer's considerations developed a minimum speed threshold v_ϖ sufficient to predict runaway in a hydrogenic plasma. This sufficient condition has a lower speed bound of the form

$$\frac{v_\varpi}{w_e}\Big|_{\mathrm{Dreicer}} \gtrsim \sqrt{\frac{3}{\mathbb{E}_\parallel}}. \tag{A5}$$

Subsequent work by Fuchs et al. (1986) agrees with Dreicer's sufficient finding; the careful reader should note that Fuchs's critical electric field E_c is confusingly *different* from Dreicer's

in just such a way that for Fuchs's definition of thermal speed, the same formula predicts the same numerical speed as Dreicer does at sufficient runaway.

In addition, Fuchs and colleagues pointed out that a more general threshold for runaway could be identified after considering energy loss and slowing down collisions. The improved *necessary* condition shown by a Langevin analysis indicated that a somewhat lower threshold could be identified, showing that the lowest speed for runaway in terms of $\mathbb{E}_\parallel$ had the form

$$\frac{v_r}{w_e}\Big|_{\mathrm{Fuchs}} = 0.9\alpha^{-1/4}\frac{v_\varpi^D}{w_e}\Big|_{\mathrm{Dreicer}} \quad \alpha = Z + 1 = 3$$
$$\mathcal{E}_{\mathrm{Fuchs}} = 3^{-1/2} \times 0.81\frac{3}{\mathbb{E}_\parallel} = 0.467\frac{3}{\mathbb{E}_\parallel}$$
$$\zeta^{\mathrm{Fuchs}} = 0.467 \quad \zeta^{\mathrm{Dreicer}} = 1, \tag{A6}$$

where the numerical factor of 0.9 comes from numerical determination of separatrices. The $\mathbb{E}_\parallel$ scaling of v_r is motivated by Fuchs et al. (1986).

Presuming that the energy $\mathcal{E}_\varpi$ found in each Wind eVDF corresponded to Fuchs's theoretical boundary necessitates $\zeta = 0.467$; such a value requires that all inventoried values summarized above as $\overline{|\mathbb{E}_\parallel|}$ would be systematically smaller than previously found: $E_\parallel^{\mathrm{Fuchs}} \simeq 0.467 E_\parallel^{\mathrm{Dreicer}}$. The experimental test summarized in Figure 21 shows that the best corroboration of the Wind $\mathcal{E}_\varpi$ determinations with the *observed* variation of $\epsilon_{Ter}(U)$ (Maksimović et al. 2020) is found with $\zeta \simeq 1.1$. Thus, by external corroboration the operational quantity $\mathcal{E}_\varpi$ of this paper is associated only with Dreicer's identification of the boundary using over a quarter million determinations. The relevance of the Fuchs hypothesis for the quantity $\mathcal{E}_\varpi$ is thus discounted by the χ^2 test discussion about Figure 21.

A subtle point for identifying these different boundaries involves the computation of their relative importance to the modification of the shape of the steady eVDF across either. The Fuchs calculation was aimed at explaining the scaling of runaway for plasmas with higher Z impurities. The one-fourth root dependence of the size of v_r was especially effective in lowering his predicted runaway boundary in plasmas with $Z = 9$ that markedly enhanced the predicted runaway flux. It may be that in hydrogenic plasmas with $Z = 1$ the sensitivity in terms of the eVDF deformation or onset is not so strident that current instrumentation is sensitive to the v_r versus v_ϖ differences. The arguments made in the text suggest that consistency between finding $\mathcal{E}_\varpi$ and linking it to $\mathbb{E}_\parallel$ is that path that leads to external validation of accuracy.

A.4. Recipe to Measure $\mathbb{E}_\parallel$ from eVDF

The inverse of the *square of the effective local thermal speed*, $w_{\mathrm{eff}}^2(v)$, needed for Equation (13) in the main text may be determined from the speed-dependent concavity profile for $\ln f(v)$ exploiting

$$\frac{1}{w_{\mathrm{eff}}^2(v)} = -\frac{1}{2}\frac{d^2\left[\ln f_c(v) + \ln\left(1 + \frac{f_h(v)}{f_c(v)}\right)\right]}{dv^2}$$
$$= \frac{1}{w_c^2} - \frac{1}{2}\frac{d^2\ln\left[1 + \frac{f_h(v)}{f_c(v)}\right]}{dv^2}, \tag{A7}$$

where $m_e w_c^2 = 2kT_c$. This approach nicely separates w_{eff}^{-2} into the constant concavity of the thermal spread of $f_c(v)$ alone and a second v-dependent correction term that reflects the kurtotic

form of $f(v)$ used in the solar wind eVDF modeling. The correction term exhibits the expected contributions from the ratio of the subcomponent distributions at the given speed.

Using Equation (9), a closed form expression for the needed expression in Equation (13) takes the form

$$\frac{w_{c\parallel}^2}{w_{\mathrm{eff}}^2(v)} = \{1 - \mathbb{RR}(v)[1 + \mathbb{Q}_1(v) - \mathbb{Q}_2(v) + \mathbb{Q}_3(v)]\}$$

$$\mathbb{RR}(v) = \frac{f_h(v)}{f_c(v)}$$

$$\mathbb{Q}_1(v) = \frac{2(v - U_c)^2}{w_{c\parallel}^2}$$

$$\mathbb{Q}_2(v) = \frac{[4(v - U_c)(v - U_h) + w_{c\parallel}^2](1 + \kappa)}{[\kappa w_{h,\parallel}^2 + (v - U_h)^2]}$$

$$\mathbb{Q}_3(v) = \frac{(2\kappa + 4)(\kappa + 1)w_{c\parallel}^2(v - U_h)^2}{[\kappa w_{h\parallel}^2 + (v - U_h)^2]^2}. \quad (A8)$$

It should be noted then that

$$\mathbb{T}(v) = \frac{1 - \mathbb{RR}(U_c)[1 + \mathbb{Q}_1(U_c) - \mathbb{Q}_2(U_c) + \mathbb{Q}_3(U_c)]}{1 - \mathbb{RR}(v)[1 + \mathbb{Q}_1(v) - \mathbb{Q}_2(v) + \mathbb{Q}_3(v)]}, \quad (A9)$$

while the dimensionless curvature takes the form

$$\mathbb{C}(v) = -\frac{1 - \mathbb{RR}(v)[1 + \mathbb{Q}_1(v) - \mathbb{Q}_2(v) + \mathbb{Q}_3(v)]}{1 - \mathbb{RR}(U_c)[1 + \mathbb{Q}_1(U_c) - \mathbb{Q}_2(U_c) + \mathbb{Q}_3(U_c)]}. \quad (A10)$$

The dimensionless $\mathbb{S}$ function is found from the identity $\mathbb{S} = \mathbb{C} + 1$.

A.5. Possible Source for Scales $\epsilon_{P_\parallel} < 0$ and $\epsilon_{P_\parallel} > 10$

The morphology of the short-scale structures with wind speed suggests that the Wind-SERM electric field analysis has detected other pressure gradients in the plasma with scales shorter than those associated with the logarithmic derivative of solar wind pressure gradients that arguably would be restricted between 2 and 3.33.

A possible source with the observed morphology are the stream−stream interactions driven by corotation that preferentially produce compressional disturbances oblique to the magnetic field in slower winds at the fixed 1 au vantage point of this Wind 3DP data set. The power shown in Figure 18, extending out to dimensionless exponents of 100, suggests the detection of gradient scales $1/50$ the half au scales associated with traditional spherical flows. These translate into scales 0.01 au in scale, compatible with structures already known to be commonplace in the 1 au solar wind (Burlaga 1995). Structures of these scales would pass over Wind in an interval of approximately 0.04 days or with a duration of 56 minutes, clearly resolvable by more than $\mathcal{O}$ (30) Wind 3DP spectra.

The likelihood that $\epsilon_{P_\parallel} < 0$ could be *physical* can be made plausible by considering a tractible pressure radial profile with superposed finite-amplitude pressure waves that would attend snow plow compressions at corotating interacting stream fronts. Convection of these quasi-standing waves in the rest frame of the density compression could produce pressure undulations or pulses that would appear to alternate about the long-wavelength pressure profile. The cycle of crest and trough of the perturbation suggests to the observer that the total pressure is alternately increasing with radius and decreasing with increasing radius. This plausible signature of compressive disturbances will generate alternating local exponent signs, depending on the amplitude of the perturbation relative to the background pressure. This likely alternation from the very same wave crests may have some bearing on the apparently
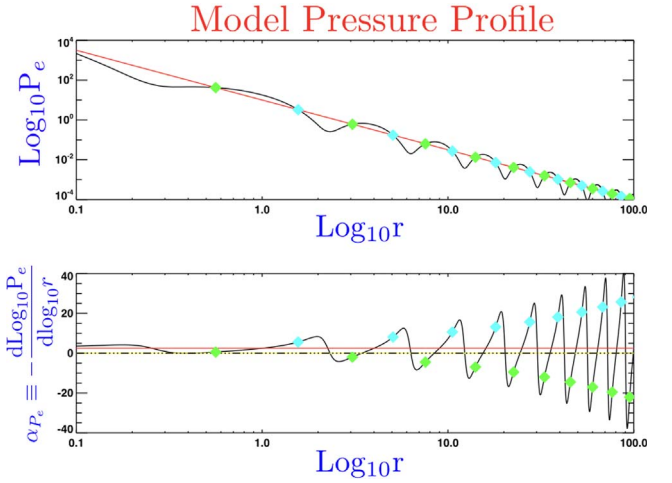
Figure 28. Illustration of impact of mesoscale pressure $P(r)$ variations superposed on the irreducible slowest profile in red, inset (T). Illustration (inset B) of α_{P_e} deduced from synthetic composite profiles in inset (T). Diamonds of different colors in the two insets identify corresponding locations of the two profiles between the insets. The cyan colored diamonds correspond to enhancements of α_P, while the green diamonds correspond to reverse gradient regimes where pressure is growing with increasing radius, the opposite behavior of the irreducible slowest profile that decreases as radius increases.

nearly identical cumulative occurrence of positive and negative sharp structures in the wind data set.

A simple model of radial pressure variations superposed on the longest scale with a radially decreasing pressure variation is used in this section to motivate the appearance of counter-intuitive radial pressure exponents that have the opposite sign and/or large absolute values compared to those expected for simple spherically symmetric solar wind solutions.

The following *illustrative* model takes the form

$$P_e(r) \simeq \frac{10}{r^{5/2}}\Big[1 + \frac{4}{5}\cos(2\pi\sqrt{r/r_o})\Big]. \quad (A11)$$

By construction, the disturbance $P_e(r)$ has a radially growing spatial wavenumber, so that the disturbances, shown in the top panel of log–log Figure 28, develop sharper and sharper crests with increasing radius, r.

On this graph paper, the logarithmic derivative definition of $\epsilon_{P_\parallel r P_e}$ reverts to minus the first derivative, with results shown in the bottom inset. The background irreducible pressure profile's exponent without perturbations is indicated by small-amplitude red curves in *both* panels, showing its constant weak positive exponent corresponding to decreasing single power-law pressure profile with increasing radius. However, as one passes over each crest of the perturbation, the local value of $\epsilon_{P_e\parallel r}$ alternately increases and decreases the estimate for $\epsilon_{P_e\parallel r}$ from the background profile. If the disturbance is large enough, these reversals can reverse the longest wavelength's radial pressure gradient exponent's sign, flipping signs between half-cycles of the perturbation. It should also be noted that this process can also give rise to pressure exponents of the same sign as that of the irreducible (red) profile, but of smaller magnitude. Looking at Figures 17 and 18, rare values of $0 < \epsilon_{P_\parallel r} < 2$ are in evidence. The dark gap around 0 in the Wind data may reflect the relatively low probability for making observations of these gradients when they pass through zero.

Being at a fixed location, Wind's situation is slightly different than this radial picture, since it is the passage of time that brings new examples to the speed bin, rather than moving

to a different radial position. It is $E_\parallel(t, \overline{U})$ that is sampled at different times. From Figure 28 this situation occurs by the spacecraft sampling the profile within the same speed bin with different $|\nabla P_e|$.

This exploration shows that the high wavenumber information in Figure 17 is not the appropriate data for corroborating with the low wavenumber limited power-law characterizations of *solar wind* pressure and temperature profiles.

A.6. Positive and Negative Scale Lengths

Logarithmic derivatives ϵ_X for a scalar physical parameter X conveniently determine the local power-law behavior of X's profile, defined by

$$\epsilon_{\chi_r} \equiv -\frac{d \ln \chi}{d \ln r}. \qquad (A12)$$

With this definition, when χ is a decreasing function of increasing r, $\epsilon_{\chi_r} > 0$; conversely, when χ is increasing with increasing r, $\epsilon_{\chi_r} < 0$.

A.7. Relationship of $\epsilon_{Pe\parallel_r}$ to ϵ_{Per}

The total pressure is related to the parallel pressure by using the anisotropy $\mathcal{A}_e$:

$$P_e = \frac{P_{e\parallel}}{3}\left(1 + \frac{2}{\mathcal{A}_e}\right). \qquad (A13)$$

Thus,

$$\frac{dP_e}{dr} = \frac{1}{3}\frac{dP_{e\parallel}}{dr}\left(1 + \frac{2}{\mathcal{A}_e}\right) - \frac{2P_{e\parallel}}{3\mathcal{A}_e^2}\frac{d\mathcal{A}_e}{dU}\frac{dU}{dr}, \qquad (A14)$$

yielding

$$\epsilon_{Per} = \epsilon_{Pe\parallel_r} - \frac{2U\overline{\beta}}{(2 + \mathcal{A}_e)\mathcal{A}_e}\epsilon_{U_r}, \qquad (A15)$$

where $\overline{\beta} \equiv \overline{d\mathcal{A}_e/dU}$ is a semiempirically known parameter given in Equation (A17).

A.8. Runaway Separatrix $\mathbb{S}$ Construction

Mathematically the construction of the $\mathbb{S}(\mathbb{E}_\parallel)$ separatrix curve requires integrating two different branches that leave an X critical point in velocity space; $\mathbb{E}_\parallel$ and T_e are parameters in this formulation (Fuchs et al. 1986). These equations include scattering off of electrons and ions. For the strahl studies reported in this paper, the relevant separatrix $\mathbb{S}(\mathbb{E}_\parallel, T_e)$ (such as the blue curves in Figure 2 or Figure 23) was constructed for each spectrum, allowing statistical comparisons (reported in the main body of the paper) of the location of the observed strahl relative to the sphere of coulomb collisional dominance (the sphere bounded by red circle at v_ϖ in Figure 23) and the closest point on the blue runaway separatrix $\mathbb{S}$ seen in the same figure.

A.9. Semiempirical Syntheses of the Wind Electron Parameters 1995–1998

1. Bulk Speed Dependence of T_e:

$$\mathrm{Log}_{10}T_e(U(\mathrm{km\ s}^{-1})) = \overline{\alpha_{Te}} + \overline{\beta_{Te}}U + \overline{\gamma_{Te}}U^2, \qquad (A16)$$

where $\overline{\alpha_{Te}} = 4.715$, $\overline{\beta_{Te}} = 0.0018$, and $\overline{\gamma_{Te}} = -1.8 \times 10^{-6}$.

2. Bulk Speed Dependence of $\mathcal{A}_e$:

$$\mathcal{A}_e(U(\mathrm{km\ s}^{-1})) = \overline{\alpha} + U(\mathrm{km\ s}^{-1})\overline{\beta}, \qquad (A17)$$

where $\overline{\alpha} \simeq 0.750$ and $\overline{\beta} \simeq 8.8 \times 10^{-4}\frac{\mathrm{s}}{\mathrm{km}}$.

3. Bulk Speed Dependence of ϵ_{Ter}:

$$(\epsilon_{Ter} - \overline{b} - \overline{m}U(\mathrm{km\ s}^{-1}))(\epsilon_{Ter} - \overline{c}) = 10^{-5}, \qquad (A18)$$

where $\overline{m} = -0.00185$, $\overline{b} = 1.27$, and $\overline{c} = 0.28 \pm 0.04$.

ORCID iDs

Jack D. Scudder ⓘ https://orcid.org/0000-0001-7975-5630

References

Berčić, L., Maksimović, M., Halekas, J., et al. 2021, ApJ, 921, 83
Burlaga, L. F. 1995, Interplanetary Magnetohydrodynamics (Oxford: Oxford. Univ. Press)
Cattell, C., Breneman, A., Dombeck, J., et al. 2022, ApJL, 924, L33
Dreicer, H. 1959, PhRv, 115, 238
Dreicer, H. 1960, PhRv, 117, 329
Drude, P. 1900a, AnP, 308, 369
Drude, P. 1900b, AnP, 306, 566
Feldman, W. C., Asbridge, J. R., & Bame, S. J. 1978, JGR, 83, 5285
Feldman, W. C., Asbridge, J. R., Bame, S. J., et al. 1975, JGR, 80, 4181
Fitzpatrick, R. 2015, Plasma Physics an Introduction (Boca Raton, FL: CRC Press), 64
Fuchs, V., Cairns, R. A., Lashmore-Davies, C. N., et al. 1986, PhFl, 29, 2931
Halekas, J., Berčić, L., Whittlesey, P., et al. 2021, ApJ, 916, 16
Halekas, J., Whittlesey, P., Larson, D. E., et al. 2020, ApJS, 246, 22
Issautier, K., Meyer-Vernet, N., Moncuquet, M., et al. 1998, JGR, 103, 1969
Landi, S., & Pantelinni, F. 2003, A&A, 400, 769
Larson, D. E., Lin, R. P., & Steinberg, J. 2000, GeoRL, 27, 157
Lemaire, J., & Scherer, M. 1971, JGR, 76, 7479
Lin, R. P., Anderson, K. A., Ashford, S., et al. 1995, SSRv, 71, 125
Maksimović, M., Bale, S. D., Berčić, L., et al. 2020, ApJS, 246, 62
Maksimović, M., Zouganelis, I., Chaufrey, J. Y., et al. 2005, JGR, 110, A09104
Meyer-Vernet, N. 2007, Basics of the Solar Wind (Cambridge: Cambridge Univ. Press)
Meyer-Vernet, N., & Issautier, K. 1998, JGR, 103, 29705
Montgomery, M. D., Bame, S. J., & Hundhausen, A. J. 1968, JGR, 116, 4999
Ogilvie, K. W., & Scudder, J. D. 1978, JGR, 83, 3776
Ogilvie, K. W., & Scudder, J. D. 1981, Solar Wind, Vol. 4 (Garching: Max-Planck-Institute), 250
Olbert, S. 1968, in Physics of the Magnetosphere, ed. R. D. L. Carovillano (Dordrecht: Reidel), 641
Pilipp, W. G., Miggenreider, H., Montgomery, M. D., et al. 1987, JGR, 92, 1075
Rosenbauer, H., Schwenn, R., Marsch, E., et al. 1977, ZGeo, 42, 561
Rossi, B., & Olbert, S. 1970, Introduction to the Physics of Space (New York: McGraw-Hill), 347
Salem, C. S., Hubert, D., Lacombe, C., et al. 2003, ApJ, 585, 1147
Salem, C. S., Pulupa, M., Bale, S. D., & Verscharen, D. 2021, arXiv:2107.08125
Scudder, J. D. 1996, JGR, 101, 13461
Scudder, J. D. 2019a, ApJ, 882, 146
Scudder, J. D. 2019b, ApJ, 885, 138
Scudder, J. D. 2019c, ApJ, 885, 148
Scudder, J. D., & Karimabdi, H. 2013, ApJ, 770, 265
Scudder, J. D., & Olbert, S. 1979, JGR, 84, 2755
Spitzer, L. J. 1967, Physics of Fully Ionized Gases (2nd ed.; New York: Wiley)
Štverák, Š., Maksimović, M., Trávníček, P. M., et al. 2009, JGR, 114, A05104
Štverák, Š., Trávníček, P. M., & Hellinger, P. 2015, JGRA, 120, 8177
Zouganelis, I. M., Meyer-Vernet, N., Landi, S., et al. 2005, ApJL, 626, L117